Doctoral Dissertation

Discovery of a gas giant planet around a low-mass dwarf: OGLE-2015-BLG-1649Lb

低質量星周りにおける巨大ガス惑星 OGLE-2015-BLG-1649Lb の発見

Masayuki Nagakane

Department of Earth and Space Science,
Graduate School of Science, Osaka University

February 3, 2020

List of Contents

Abstract

We report the discovery of an exoplanet from the analysis of the gravitational microlensing event OGLE-2015-BLG-1649 that challenges the core accretion model of planet formation and appears to support the disk instability model. The planet/host-star mass ratio is $q = 7.2 \times 10^{-3}$ and the projected separation normalized to the angular Einstein radius is $s = 0.9$. We conducted high-resolution follow-up observations using the Infrared Camera and Spectrograph (IRCS) camera on the Subaru telescope and are able to place an upper limit on the lens flux. From these measurements we are able to exclude all host stars greater than or equal in mass to a G-type dwarf. We conducted a Bayesian analysis with these new flux constraints included as priors resulting in estimates of the masses of the host star and planet. These are $M_{\rm L} = 0.34 \pm 0.19\,M_\odot$ and $M_{\rm p} = 2.54^{+1.48}_{-1.39}\,M_{\rm Jup}$, respectively. The distance to the system is $D_{\rm L} = 4.23^{+1.51}_{-1.64}\,{\rm kpc}$. The projected star–planet separation is $a_\perp = 2.07^{+0.65}_{-0.77}\,{\rm au}$. The estimated relative lens–source proper motion, $\sim 7.1\,{\rm mas\,yr^{-1}}$, is fairly high and thus the lens can be better constrained if additional follow-up observations are conducted several years after the event.

1 Introduction

1.1 Planet Formation Theory

More than 4100 exoplanets have been confirmed since the discovery of the first exoplanet orbiting a main-sequence star, 51 Peg b, in 1995 (Mayor & Queloz, 1995). The features of these exoplanets are much different from the solar system. There are terrestrial planets (Mercury, Venus, Earth, Mars), gas giants (Jupiter, Saturn), and ice giants (Uranus, Neptune) in the solar system. The standard core accretion model (Safronov, 1972; Hayashi et al., 1985; Lissauer, 1993) which is popularly believed as a planet formation theory is based on the solar system. However, some problems still remain in this theory. The brief summary of this theory is as follows (Figure 1).

1. Protoplanetary disk, which is composed of mainly hydrogen and helium with a mass of $\simeq 0.01 - 0.02\,M_{\rm Host}$, is formed around the host star.

2. Dust grains ($\sim$ μm) in the protoplanetary disk are aggregated at the mid-plane and $\sim$ km sized planetesimals are formed (Figure 1 (a)).

3. Collisions and growth of planetesimals lead to the formation of protoplanets.

4. **Formation of terrestrial planets**: Inside of "snow-line" (Ida & Lin, 2004b; Laughlin et al., 2004; Kennedy et al., 2006), protoplanets become Mars-size and they collide with each other (Figure 1 (b)).

5. **Formation of gas giants**: Protoplanets reach sufficient mass ($\gtrsim 10\,M_\oplus$) to capture the gas around them and grow into gas giants outside of the "snow-line" (Figure 1 (c) – (d)).

6. **Formation of ice giants**: In the region that far away from the host star, protoplanets grow slowly and they become $M \gtrsim 10\,M_\oplus$ after the gas has dispersed at late time (Figure 1 (d)).

The dust grain with a radius of d orbiting at a radius of a away from the host star receive the energy of

$$E_{receive} = \frac{\pi a^2 L}{4\pi r^2}, \tag{1}$$

where L is the luminosity of the host star. The thermal radiation from the dust grain can be written as

$$E_{radiate} = 4\pi d^2 \sigma T^4, \tag{2}$$

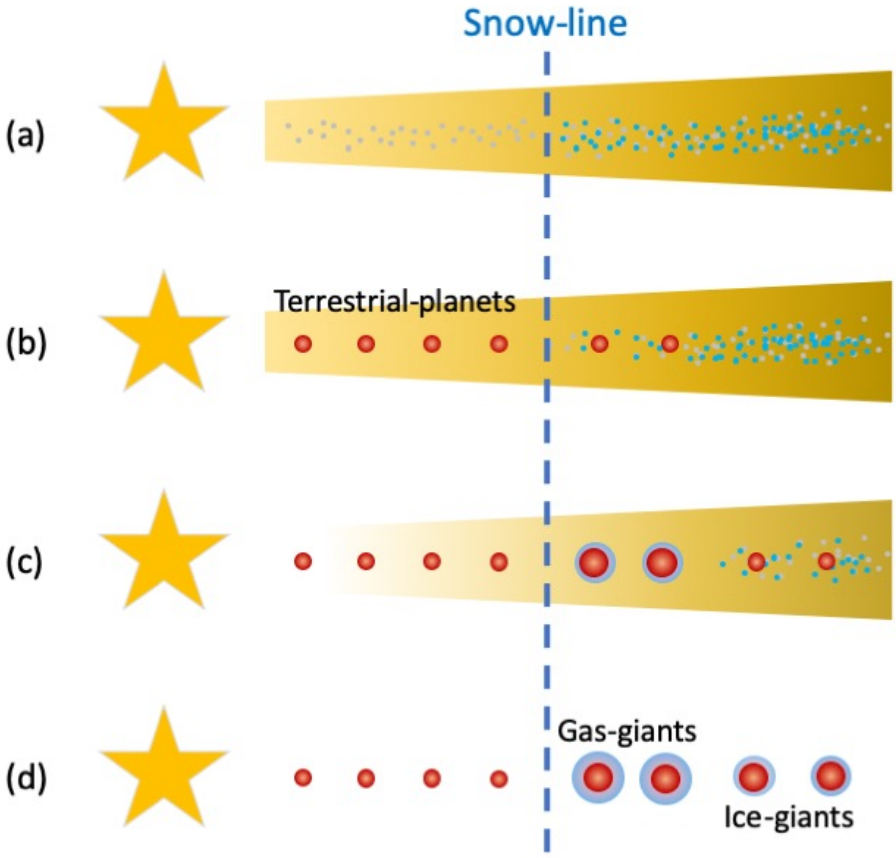

Figure 1: Schematic diagrams of the standard core accretion model. The diagrams are organized by chronological order from top to bottom.

where σ is the Stefan–Boltzmann constant and T is the surface temperature of the dust grain. Therefore, the equilibrium temperature is approximately described as

$$T_{eq} = 280 \left(\frac{r}{1\,\mathrm{au}}\right)^{-1/2} \left(\frac{L}{L_\odot}\right)^{1/4} \mathrm{K}. \tag{3}$$

The "snow-line" is the place that the protoplanetary disk becomes cold for water may condense into solid ice grains. The snow-line is located at $\sim 2.7\,\mathrm{au}\,(M/M_\odot)^2$ for a main sequence star (Ida, & Lin, 2004a). The scaling factor of this depends on the stellar mass–luminosity relation as a function of stellar age. Therefore, the location of snow-line at the time of planet formation (typically $\sim 10^6\,\mathrm{yr}$) is described as $\sim 2.7\,\mathrm{au}\,(M/M_\odot)$ (Kennedy, & Kenyon, 2008).

In the region outside of the snow-line, the ice grains become one of the component materials of the planets. Consequently, the mass of the planet core will be larger than that inside of the snow-line. If the planet core becomes massive enough to start a rapid gas accretion, the planet continues to grow until the materials around the planet have disappeared. As a result, the gas giant planet with a mass of $> 100\,M_\oplus$ is formed. The formation time for the planet with a given mass extends approximately proportional to a^3, where a is the semi-major axis of the planet. Therefore, in the region far away from the snow-line, the mass of the planet core probably not be able to become $\sim 10\,M_\oplus$ before the gas in the protoplanetary disk has dispersed.

This core accretion theory predicts that giant planets formed at the outer region than terrestrial planets and favors almost circular orbits. There are many discoveries of "Hot Jupiters" which are gas giants orbiting very close to the host star. 51 Peg b (Mayor & Queloz, 1995) is one of the Hot Jupiters with a mass of $0.46\,M_{\mathrm{Jup}}$ orbiting only $0.051\,\mathrm{au}$ away from the host star. The standard core accretion model does not predict such exoplanets. The formation theory of these exoplanets is not well known but the migration model (Lin et al., 1996) is the best guess at the moment. "Eccentric Jupiters" which have high orbital eccentricity are also discovered. Moreover, super-Earth mass exoplanets exist at the semi-major axis of $0.1\,\mathrm{au}$. The innermost planet in the solar system, Mercury, has the semi-major axis of $0.4\,\mathrm{au}$ and the gas giants, Jupiter and Saturn, are orbiting beyond $5\,\mathrm{au}$ with an almost circular orbit. Therefore, the standard core accretion model based on the solar system cannot explain the formation of these exoplanets. The migration model is the best guess to explain the formation of Hot Jupiters (Lin et al., 1996) and super-Earth mass planets around $0.1\,\mathrm{au}$ (Ida, & Lin, 2010).

In the massive protoplanetary disk, many gas giants are formed and then, their orbits are perturbed by their own gravitation (Rasio, & Ford, 1996; Weidenschilling, & Marzari, 1996; Lin, & Ida, 1997). Some planets are ejected from the system and

the orbits of the remaining planets become elliptical. This mechanism is one of the formation theory of Eccentric Jupiters (Ida et al., 2013).

On the other hand, the low-mass protoplanetary disk has much less materials for planets and the growth rate of protoplanets is small. Therefore, the gas giants may be difficult to form in the low-mass protoplanetary disk (Ida, & Lin, 2005).

The disk instability model is another scenario for the gas giant formation (Cameron, 1978; Boss, 1997). This model states that a protoplanetary disk is fragmented by its own gravity, and then the fragments collapse into giant gaseous protoplanets. According to this theory, the gas giant planets that have an orbit with high eccentricity can form directly. Moreover, this mechanism is also predicted to occur around M-dwarfs (Boss, 2006). However, it is difficult to describe the formation of terrestrial planets and ice giants with this theory.

1.2 Observation Methods

There are four main methods to detect exoplanets:

Radial Velocity method

The radial velocity method, also called the Doppler method, detects the variation of line-of-sight velocity of the host star with the Doppler shift (Butler et al., 2006). If the planets around their host star move in a Keplerian motion around their barycenter, and the spectral lines on the stellar spectrum shifts with time. This method can measure only line-of-sight velocity, and cannot measure the orbital inclination i. Therefore, only the lower limit of mass $M_{\rm p}$, $M_{\rm p}\sin i$ is able to be inferred. This method is sensitive to planets with higher masses and closer orbits because the massive planet perturbs its host star more than the low-mass planet. The precision of $\sim 10\,{\rm m/s}$ is required for the Sun–Jupiter system, and $\sim 0.1\,{\rm m/s}$ is required for the Sun–Earth system. Echelle SPectrograph for Rocky Exoplanets and Stable Spectroscopic Observations (ESPRESSO; Pepe et al. 2014) that is a new-generation echelle spectrograph mounted on the Very Large Telescope (VLT) would be able to attain the precision of a few cm/s. 861 planets are detected by this method including the first detection of exoplanet 51 Peg b (Mayor & Queloz, 1995).

Transit method

The transit method detects the planet eclipse, i.e., the planet crosses in front of its host, blocking some of the light from the star (Borucki et al., 2011). The cross-section area of the transiting exoplanet in units of that of its host star

can be obtained from the ratio of dimming. The first measurement of planet eclipse is HD209458 b which had already detected by the radial velocity method (Charbonneau et al., 2000). They found the period synchronized with a known orbital period (~ 3.5 days). It is very significant that we can measure the actual planet's mass rather than only a lower limit by the transit. The probability of the transit is higher for closer orbit and enlarger planet radius, i.e., likely to be a massive planet. The *Kepler* space mission (Borucki et al., 2010; Batalha et al., 2013) have detected hundreds of exoplanets and thousands of candidates out to ~ 1 au from their host stars. About 3/4 of all detected exoplanets, 2959 planets, have been detected by this method.

Direct Imaging method

The direct imaging method detects the thermal radiation of planets directly. This method requires high spatial resolution and high contrast to separate radiation from a planet and a host star. Adaptive Optics (AO) is used to reduce the effect of wavefront distortions, high-contrast imaging and coronagraph are used to increase the contrast. This method is sensitive to massive planets that orbit far from their host stars (Macintosh et al., 2015). 131 planets are detected so far.

Gravitational Microlensing method

When a background source star is closely aligned with a foreground lens star, the gravity of the lens bends the light from the source star to create unresolved images of the source, yielding an apparent magnification of the source star brightness. The relative motion of the lens and source stars result in a light curve with brightness changing as a function of time. If the lens star has a planetary companion lying close to one of the source images, the gravity of the planet perturbs the image, producing an anomaly in the observed light curve. Gravitational Microlensing is sensitive to planets (Bennett & Rhie, 1996) orbiting faint and/or distant stars and exhibits unique sensitivity to planets with orbital radii of $1-6$ au, just outside the snow-line, with masses down to that of Mercury. Contrary to the other planet detection methods mentioned above, gravitational microlensing does not rely on any light from the host star. Since the first discovery of exoplanets by gravitational microlensing (Bond et al., 2004), 101 planetary microlensing events have been found.

These four methods detected many different types of planetary systems (Figure 2). According to Figure 2, the exoplanets similar to the solar system planets are not much discovered except for Jupiter so far. Collecting larger samples of exoplanets and improvement of the statistic is important to constrain the planet formation theory.

Furthermore, the distribution of various exoplanet populations as a function of their host's location within the Galaxy has not been revealed. It is because these planetary exploration methods do not have sensitivity for distant planetary systems from the Earth except for the gravitational microlensing method. Therefore, systematic analysis of many microlensing events is important to probe the planet distribution in the Galaxy.

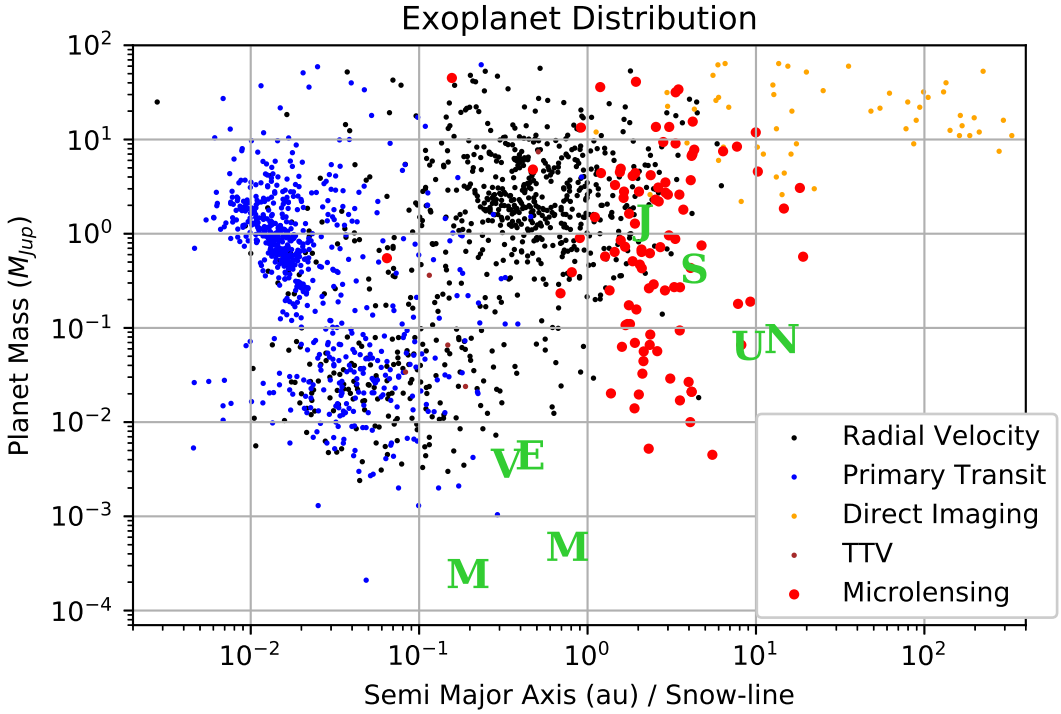

Figure 2: Distribution of known exoplanets. The vertical axis and horizontal axis correspond to the planet mass and the semi-major axis normalized by the snow-line which is assumed to depend on the host star mass as $\sim 2.7\,\mathrm{au}\,(M/M_\odot)$ (Kennedy, & Kenyon, 2008), respectively. Green letters indicate the solar system planets. The values are from http://exoplanet.eu.

The results of the statistical analysis of planets discovered from the MOA-II microlensing survey conducted during the 2007 – 2012 period suggest that cold exo-Neptunes are the most common type of planets beyond the snow line (Suzuki et al., 2016, 2018). These studies used the planet–host mass ratio, the primary observable in all planetary microlensing events, to determine the exoplanet frequency. Other

information is needed to obtain the actual masses of the system bodies from these measurements. A statistically robust sample of masses of planets beyond the snow line is important because it may permit more meaningful results to be drawn from a demographic understanding of exoplanets. In particular, such measurements hold the potential to provide a crucial calibration of planet formation theory.

The brief history and basics of gravitational microlensing are described in Section 2. The discovery of a planet found from the analysis of the microlensing event, OGLE-2015-BLG-1649, is described in Section 3 The lens mass of OGLE-2015-BLG-1649L is estimated from the angular Einstein radius together with the excess flux measurement in the high-resolution images obtained from follow-up observations using the Subaru telescope with an AO system. This section is published as Nagakane et al. (2019). The contents have not been made any changes except for the section numbers. Therefore, there are some overlapping throughout this thesis. The discussion and conclusion are given in Section 4. Appendix A presents the discovery of a planetary system in the Galactic bulge in the high amplification microlensing event MOA-2012-BLG-505 published as Nagakane et al. (2017). The further discussions from Nagakane et al. (2017) and Nagakane et al. (2019) are described in Appendix B. This thesis is written in the modified AAS (the American Astronomical Society) format.

2 Gravitational Microlensing

2.1 Brief History

According to Einstein's general theory of relativity, a gravitational field bends a light. The light from a source object is bent by gravitational fields of lens objects just like a lens due to this effect. This phenomenon is known as gravitational lensing. If the lens object is a galaxy or a cluster of galaxies that is massive enough to produce multiple images, arcs or rings, it is called strong gravitational lensing. On the other hand, if the lens object is a star or a planet, the separation between images is too small to be resolved and it is known as gravitational microlensing. However, microlensing is identified as a temporal magnification of the source object. The meaning is that the microlensing method does not measure the lens flux, but measure the source flux. Therefore, this method can detect dark objects, such as black holes, white dwarfs, brown dwarfs and planets including free floating planets (FFPs).

Gravitational lensing was first mentioned by Chwolson (1924). He remarked that the image of the source object will be a ring shape when the source object, the lens object, and the observer lie in a straight line. Thereafter Albert Einstein quantified the amount of magnification from the lens equation (Einstein, 1936). In his paper, he noted that, "Of course, there is no hope of observing this phenomenon directly." because the alignment scarcely happens and the separation angle of the source images is too small to be observed. Moreover, he said that, "there is no great chance of observing this phenomenon, even if dazzling by the light of the much nearer star B is disregarded" for observing apparent amplification by gravitational lensing.

About thirty years later, Sidney Liebes, Jr. considered the lens action of the exoplanets (Liebes, 1964). He found that, "the primary effect of planetary deflectors bound to the stars other than the sun will be to slightly perturb the lens action of these stars." He also mentioned about the lens action caused by FFPs. The conclusion is that it is difficult to detect such events because there are few events caused by FFPs in detectable events, and also if it occurs, the duration is weak and has a short time (perhaps a few hours).

About twenty years after from Liebes' report, the method for observing many stars and discovering the gravitational microlensing phenomena was proposed by Bohdan Paczyński as a way to find MAssive Compact Halo Objects (MACHOs) in the Galactic halo that were considered one of candidates of dark matter at the time (Paczynski, 1986). Moreover, Mao & Paczyński (1991) predicted that exoplanets could be discovered by using the gravitational microlensing method. According to previous research, the probability that the microlensing events happen to any given bulge star

at any particular time is $\sim 10^{-6}$. Therefore, it is very difficult to observe such events with photographic plates. However, the CCD camera allowed us to monitor hundreds of millions of source stars and detect the microlensing phenomena. At long last, in 1993, the microlensing event was first detected in the direction of the Large Magellanic Cloud (Alcock et al., 1993a) by the MACHO collaboration (Alcock et al., 1993b) and EROS collaboration (Aubourg et al., 1993). Almost at the same time, the Optical Gravitational Lensing Experiment (OGLE) collaboration (Udalski et al., 1992) discovered the first microlensing event towards the Galactic Bulge (Udalski et al., 1993). The planetary microlensing event had not been discovered for a long time. After a decade from these microlensing events, in 2003, the OGLE collaboration and the Microlensing Observations in Astrophysics (MOA; Bond et al., 2001; Sumi et al., 2003) collaboration finally detected the first planetary microlensing event, OGLE 2003-BLG-235 / MOA 2003-BLG-53 (Bond et al., 2004). These days, about 2000 microlensing events are discovered annually and roughly 10 of these events have the unmistakable planetary signals.

2.2 Basic Principle of The Gravitational Microlensing

2.2.1 Single Lens

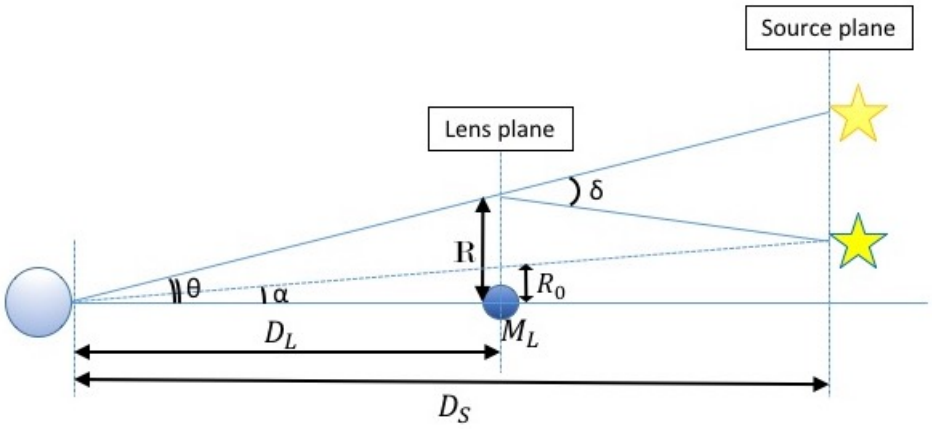

Figure 3: Conceptual diagram of microlensing. The lens and source star are located at $D_{\rm L}$ and $D_{\rm S}$ away from the Earth, respectively.

Gravitational microlensing occurs when the lens star is almost aligned with a

background source star. Figure 3 is a conceptual diagram of microlensing. Let us assume each lens is a point mass and the source is a point source, and the lens and source star are located at $D_{\rm L}$ and $D_{\rm S}$ away from the Earth, respectively. We define the angles, θ, α, δ as shown in Figure 3, which can be given by the following equations:

$$\theta = \frac{R}{D_{\rm L}}, \tag{4}$$

$$\alpha = \frac{R_0}{D_{\rm L}}. \tag{5}$$

Therefore, we can also obtain the equation,

$$D_S\,\theta = D_{\rm S}\,\alpha + D_{\rm S}\,\delta\,(1-x), \tag{6}$$

where $x \equiv D_{\rm L}/D_{\rm S}$. According to Einstein's general theory of relativity, the light passing at the distance of R away from the mass point with a mass of M is bent by angle

$$\alpha(R) = \frac{4GM}{Rc^2} \quad (R \gg r_g \equiv \frac{2GM}{c^2}), \tag{7}$$

where c is the speed of light, G is the gravitational constant, and r_g is Schwarzschild radius. With the equation of (4), (5) and (7), the equation of (6) yields

$$R^2 - R_0\,R - R_E^2 = 0, \tag{8}$$

where $R_{\rm E}$ is the Einstein radius, and this equation is called the lens equation. The Einstein radius is defined as

$$R_E \equiv D_{\rm L}\,\theta_{\rm E} \equiv \sqrt{\frac{4GM}{c^2}\,D_{\rm S}\,x\,(1-x)} \tag{9}$$

$$\simeq 2.6\,{\rm AU}\left(\frac{M}{0.5M_\odot}\right)^{1/2}\left(\frac{D_{\rm S}}{8\,{\rm kpc}}\right)^{1/2}\left(\frac{x\,(1-x)}{0.2}\right)^{1/2}, \tag{10}$$

where $\theta_{\rm E}$ is the angular Einstein radius. Equation (8) has two solutions:

$$R = \frac{R_0 \pm \sqrt{r_0^2 + 4R_{\rm E}^2}}{2}. \tag{11}$$

It is difficult to resolve these images due to a typical size of the angular Einstein radius of

$$\theta_{\rm E} \simeq 391\,\mu as\left(\frac{M}{0.5M_\odot}\right)^{1/2}\left(\frac{D_{\rm S}}{8\,{\rm kpc}}\right)^{1/2}\left(\frac{x\,(1-x)}{0.3}\right)^{1/2}. \tag{12}$$

The observed brightness of lensed images is the surface brightness integrated over the image area because the surface brightness is conserved. Therefore, the observed magnification can be written as

$$A = \left| \left(\frac{R}{R_0} \frac{dr}{dr_0} \right) \right| = \left| \frac{R^4}{R^4 - R_{\rm E}^4} \right|. \tag{13}$$

The total magnification is the sum of the magnification of two images as

$$A = A_1 + A_2 = \frac{u^2 + 2}{u\sqrt{u^2 + 4}}, \tag{14}$$

where u is the normalized lens–source separation

$$u \equiv \frac{R_0}{R_{\rm E}} = \frac{\alpha}{\theta_{\rm E}}. \tag{15}$$

In general, because the lens and source star has some velocity relative to the observer, u depends on time and so does A. If we assume the lens and source stars are moving inertially with respect to the observer, we can describe the time-dependent lens–source separation as

$$u(t) = \sqrt{u_0^2 + \left(\frac{t - t_0}{t_{\rm E}} \right)^2}, \tag{16}$$

where u_0 is the minimum impact parameter, t_0 is the time when $u = u_0$, $t_{\rm E}$ is the Einstein radius crossing time, called the event timescale or Einstein timescale

$$t_{\rm E} \equiv \frac{R_{\rm E}}{v_\perp}, \tag{17}$$

and $v_\perp$ is the lens–source relative transverse velocity. Substituting this into the equation (14), the time-dependent magnification is written as

$$A(t) = \frac{y^2 + u_0^2 + 2}{\sqrt{y^2 + u_0^2}\sqrt{y^2 + u_0^2 + 4}}, \tag{18}$$

where $y \equiv (t - t_0)/t_{\rm E}$. According to this equation, it can be seen that the light curve is symmetric in t_0, and its peak magnification increase with decreasing value of u_0 (Figure 4).

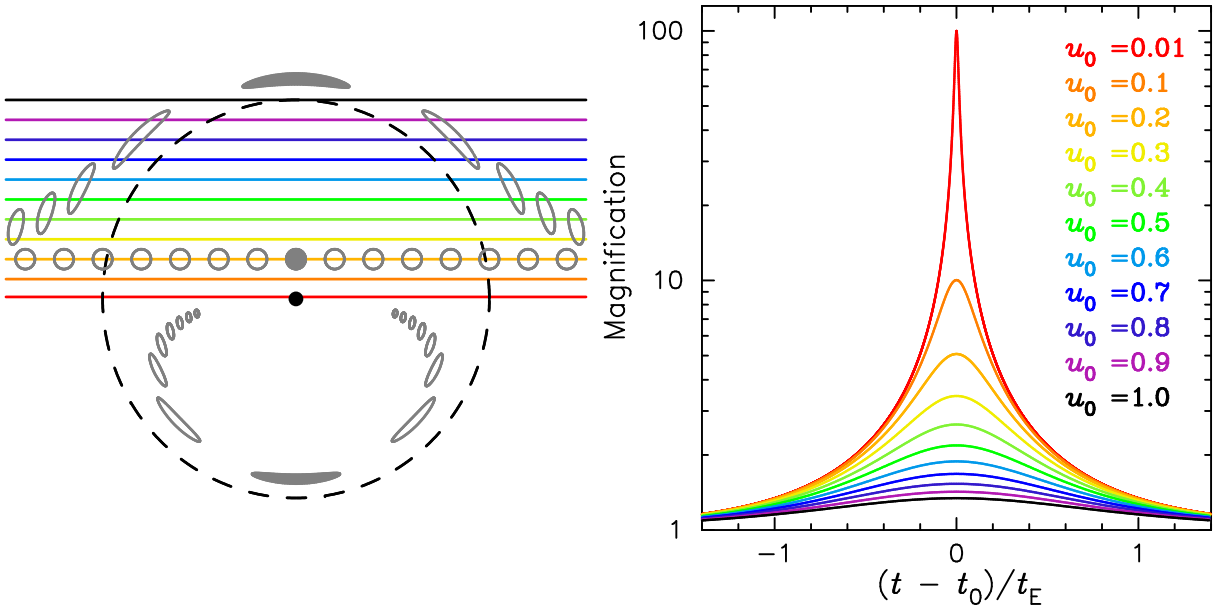

Figure 4: (Left) The gray circle and ellipses are the source position with $u_0 = 0.2$ and the two images that are created, respectively. The other circles and ellipses indicate the source position and images at different times for a trajectory with $u_0 = 0.2$. (Right) Theoretical microlensing light curves with various value of u_0. The colors are corresponding to the ones in left panel.

2.2.2 Binary Lens

When the lens star has stellar or planetary companions, the light curve shape differs from that of the single lens. Such microlensing events are called as binary lens events. We can derive the lens equation for the binary lens by modifying equations in Section 2.2.1. Defining a dimensionless vector of the source position $\boldsymbol{u} \equiv \boldsymbol{\alpha}/\theta_{\rm E}$, and the image positions $\boldsymbol{y} \equiv \boldsymbol{\theta}/\theta_{\rm E}$. The lens equation is derived as

$$\boldsymbol{u} = \boldsymbol{y} - \sum_{i=1}^{2} \epsilon_i \frac{\boldsymbol{y} - \boldsymbol{y}_{m,i}}{|\boldsymbol{y} - \boldsymbol{y}_{m,i}|^2}, \tag{19}$$

where $\epsilon \equiv m_i / \sum_{i=0}^{n} m_i$, m_i and $\boldsymbol{y}_{m,i}$ are the mass and position of ith lens, respectively. The magnification of i-th image is written as the inverse of the Jacobian of the lens equation,

$$A_i = \frac{1}{\det J}, \quad \text{where } J = \left(\frac{\delta \boldsymbol{u}}{\delta \boldsymbol{y}_i} \right). \tag{20}$$

Therefore, the total magnification is given by

$$A = \sum_i A_i. \tag{21}$$

According to equation (20), the magnification diverges to infinity if $\det J = 0$. The source position where the magnification becomes infinity is called caustic. The assemblage of the caustics mapped in the lens plane by the lens equation is called the critical curve. There are three cases of caustic depends on planet/host-star mass ratio q and projected separation normalized by the Einstein radius s. If $s < 1$, $s \simeq 1$, and $s > 1$, there are three, one, and two closed-loop of caustics (Figure 5). A caustic near the center of lens mass is called a central caustic and the others are called planetary caustics. When the source star passes close to the caustic, the light-curve deviates from single-lens light-curve. This deviation is called an anomaly which is very important to detect planets.

In general, the size of central and planetary caustics are in proportion to q and $\sqrt{q}$, respectively. The shapes of central caustic with s and $1/s$ become similar when the planet mass is small enough and the planet is located away enough from the Einstein radius (Figure 6). Therefore, if the source trajectory crosses only the central caustic as is common in high-magnification events, it is difficult to distinguish these models. This is well known as a close–wide degeneracy.

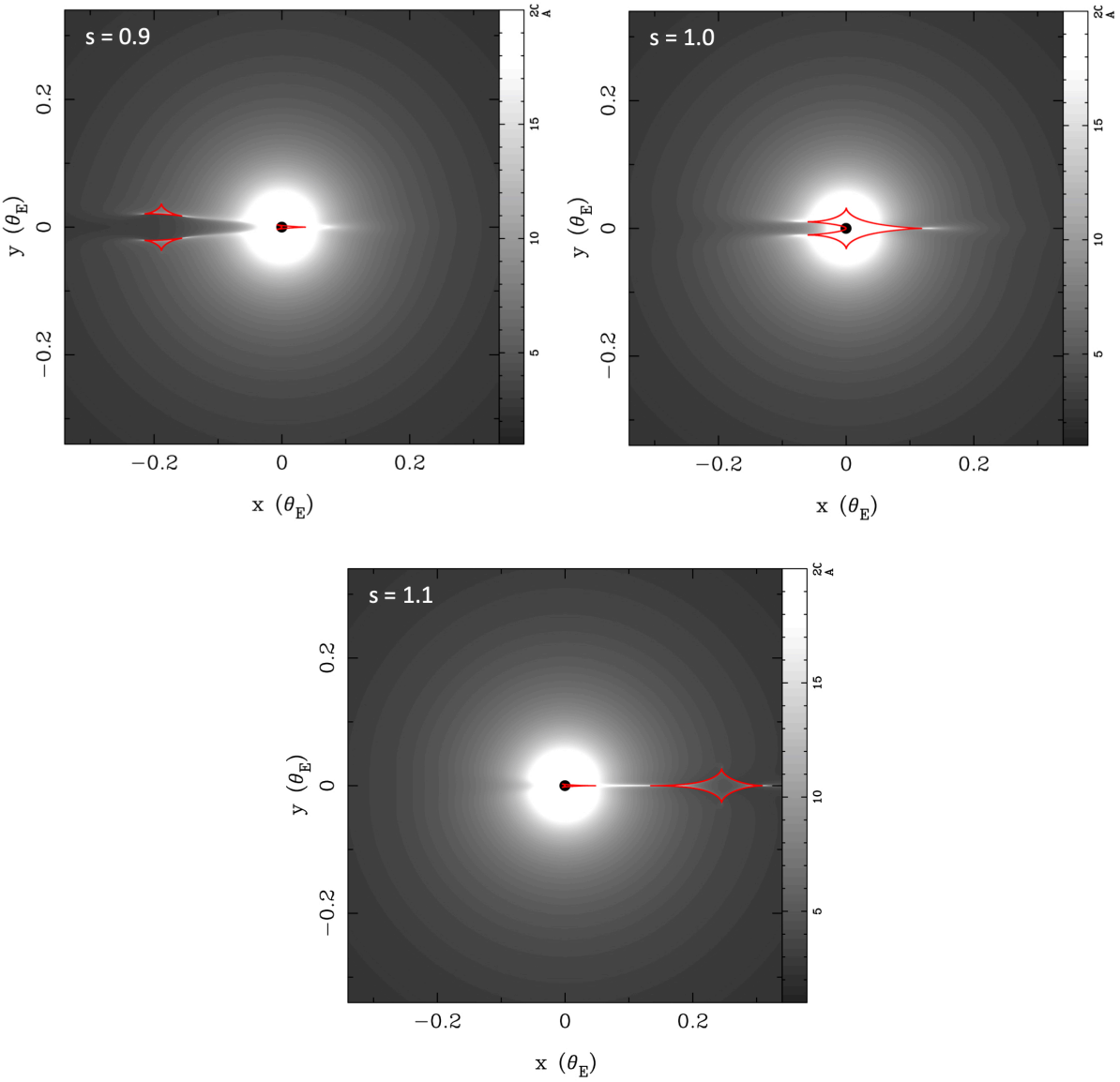

Figure 5: Caustic geometries for a planetary lens with mass ratio $q = 5 \times 10^{-4}$ with various separations s indicated by the red curves. The magnification map is represented in gray scale.

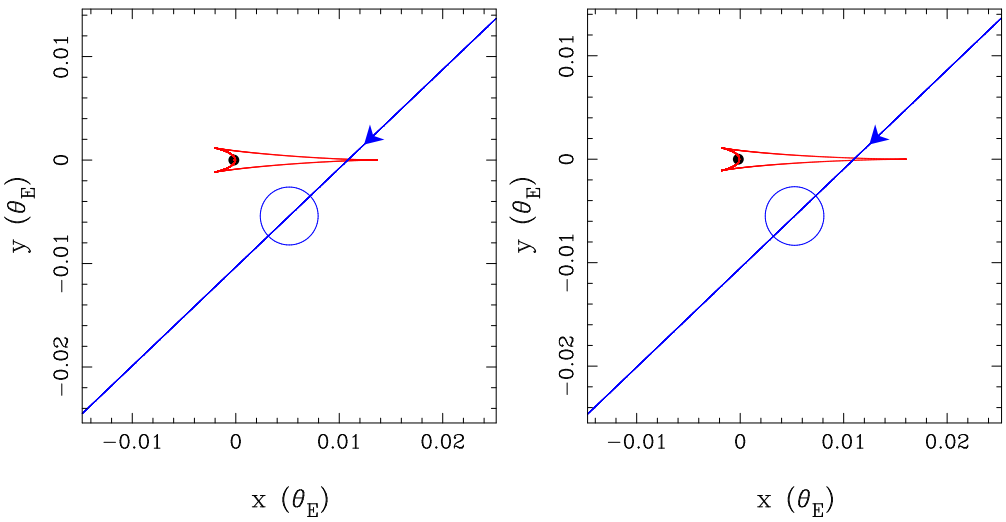

Figure 6: Caustic geometries for the close (left) and wide (right) models (Nagakane et al., 2017).

2.2.3 Higher Order Effects

The previous section assumed a point source model but this assuming is not true in some cases. Some microlensing events have higher order effects that perturb their light-curves. If these effects are detected, we are able to constrain the uncertainties of the microlensing parameters.

Finite Source Effect

If the source star crosses or approaches closely to the caustic, we cannot neglect the finite size of the source star (Figure 7). It is because of the magnification change largely in the size of the source. This effect is called a finite source effect. In the light-curve modeling, we introduce an additional parameter, ρ, the size of the source star in units of the angular Einstein ring radius as

$$\rho \equiv \frac{\theta_*}{\theta_{\rm E}}, \tag{22}$$

where θ_* is the angular source star radius. Even in the single lens event, we cannot neglect this effect when the lens star passes very close to the source star (Choi et al., 2012). We can estimate the value of θ_* from the observed source magnitude and color (Boyajian et al., 2014; Fukui et al., 2015). Therefore, $\theta_{\rm E}$ is obtained

from the detection of the finite source effect and we are able to obtain the relation between the lens mass and the distance as

$$\theta_{\rm E} \equiv \left(\frac{4GM}{c^2 D_{\rm rel}} \right)^{1/2}, \tag{23}$$

where $D_{rel}^{-1} \equiv D_{\rm L}^{-1} - D_{\rm S}^{-1}$. We can also obtain the lens–source relative proper motion $\mu_{\rm rel}$ by combining the measurement of $\theta_{\rm E}$ with the event timescale $t_{\rm E}$ as

$$\mu_{\rm rel} \equiv \frac{\theta_{\rm E}}{t_{\rm E}}. \tag{24}$$

Note that this is the geocentric relative proper motion that including the Earth's motion relative to the Sun.

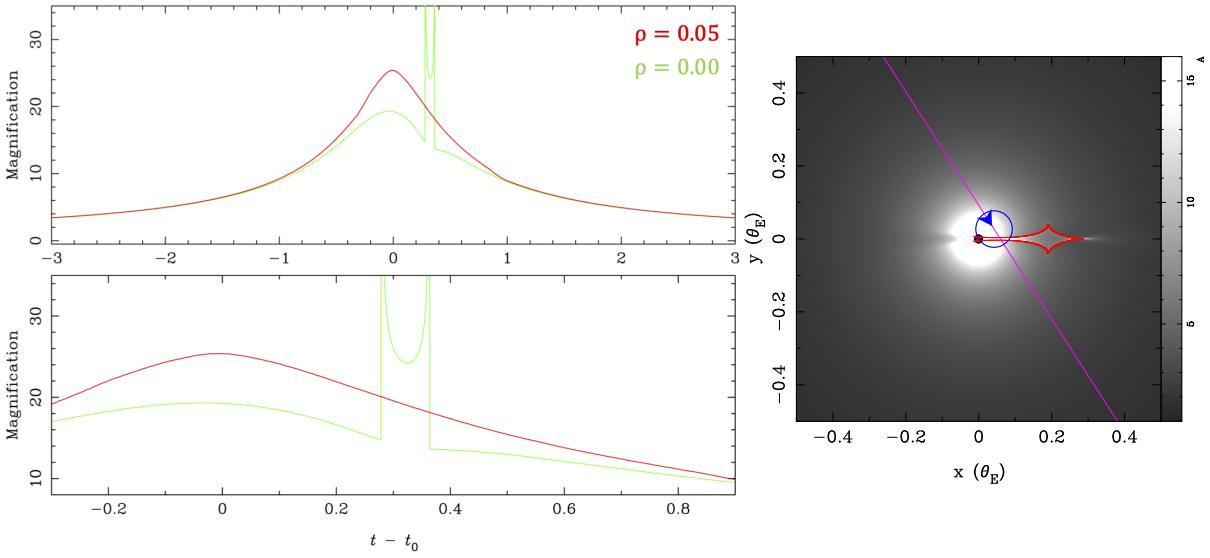

Figure 7: (Left) Light-curves of planetary microlensing event with $q = 10^{-3}$ and $s = 1.1$. The red and green lines indicate that the light-curves with and without the finite source effect, respectively. (Right) Caustic geometry with magnification map. The red curve indicates caustic and the blue line shows the source trajectory with respect to the lens system. The blue circle indicates the source star size. The magnification map is represented in gray scale.

Microlensing Parallax

We have assumed that the lens–source proper motion is approximately on a straight line and the microlensing parameters, u_0, t_0, and $t_{\rm E}$ are constant in previous sections. However, the trajectory is more complicated and these parameters change along with the relative position of observers, actually. If we measure the microlensing event from two separated locations in the observer's plane, a deviation of the light-curve can be detected. When we detect such effect, we can measure additional physical parameters $\pi_{\rm E,E}$ and $\pi_{\rm E,N}$ which are two components in the East and North directions of the relative parallax vector, $\boldsymbol{\pi}_{\rm E}$, between the source and the lens stars, respectively. There are three microlensing parallax effects: orbital parallax, satellite parallax, and terrestrial parallax. If the event timescale $t_{\rm E}$ is relatively longer (typically $t_{\rm E} > 50$ days), the effect of the orbital motion of the Earth cannot be ignored, which is called orbital parallax. Figure 8 shows an example of the difference of the light-curve and the source trajectory between the non-orbital parallax and orbital parallax models. Orbital parallax is defined as

$$\pi_{\rm E} \equiv \frac{\rm au}{\theta_{\rm E}\, D_{rel}} = \frac{\theta_{\rm E}}{\kappa M_{\rm L}}, \quad \text{where } \kappa \equiv \frac{4G}{c^2 {\rm AU}} \simeq 8.1\, \frac{\rm mas}{M_\odot}. \tag{25}$$

When the microlensing event is observed from the Earth and satellite, especially the observers are separated by a significant fraction of an Einstein ring, we are also able to obtain the parallax vector $\boldsymbol{\pi}_{\rm E}$. The difference of observers' locations gives rise to a difference in the peak time and the magnification at the peak. Satellite parallax is defined as

$$\boldsymbol{\pi}_{\rm E} = \frac{\rm au}{D_\perp} \left(\frac{\Delta t_0}{t_{\rm E}}, \Delta u_0 \right), \tag{26}$$

where Δu_0 and Δt_0 are the differences in the minimum impact parameters and the peak time between the Earth and satellite, respectively.

Terrestrial parallax can be detected when the magnification of the event is extremely high (typically $A_{MAX} \gtrsim 1000$). In such events, we are able to measure u_0 and t_0 very precisely if the high cadence observations are conducted at the peak magnification time. Since the source star lies very close to the lens star in the extremely high-magnification event, Δu_0 and Δt_0 can be also observed from the observatory at the different places on the Earth.

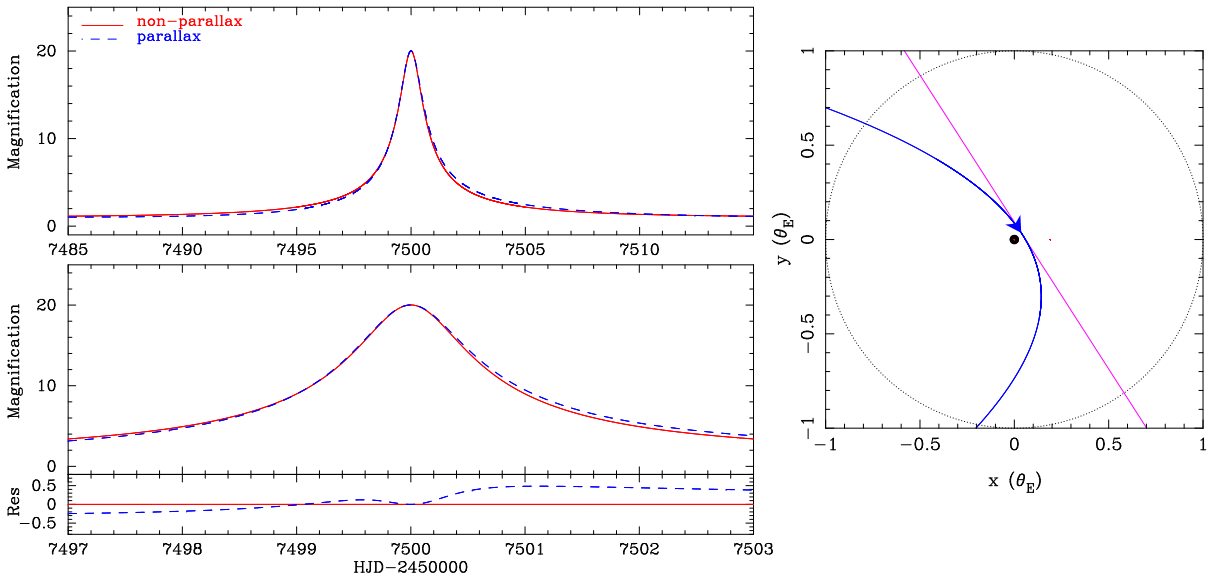

Figure 8: The light-curve (left) and the source trajectory (right) representing the orbital parallax effect. Bottom panel of left figure shows the enlarged view around the peak and the residual from the non-orbital parallax model. The black dotted circle in the right figure corresponds to the Einstein ring. The red and magenta lines indicate the both without orbital parallax effect. The blue dotted and solid lines indicate the both with orbital parallax effect.

If we detect both of these higher order effects, we are able to obtain two different mass–distance relations from $\theta_{\rm E}$ and $\pi_{\rm E}$. These two relations allow us to resolve the degeneracy of the lens mass and distance. The finite source effect can be detected commonly ($\sim$ 90%) in the binary and planetary microlensing events. However, the measurement of microlensing parallax is relatively rare ($\sim$ 30%) for events with ground-based observations due to the short baselines between observatories, daily phase differences at observatory sites, and bad observing conditions that may frustrate these time-critical measurements. If the finite source effect and/or the microlensing parallax are not detected, the Bayesian analysis will be conducted to estimate the physical parameters of the lens system.

2.2.4 Lens Flux

The microlensing parameters detected as light-curve deviations were described in the previous sections. Besides these, the flux from the lens star can put a restriction on the uncertainties of the physical parameters. When the lens flux, $F_{\rm L}$, is obtained by the observations, we can derive the mass–distance relation:

$$F_{\rm L}(\lambda) \equiv \frac{L(\lambda, M_{\rm L})}{4\pi D_{\rm L}^2}, \tag{27}$$

where $L(\lambda, M_{\rm L})$ is the mass–luminosity relation as a function of passbands, $M_{\rm L}$ is assumed to be dominated by the host star of the lens system. The lens flux can be obtained even if the magnification event is over. Therefore, we are able to determine the lens mass and distance uniquely by using the lens flux, $F_{\rm L}$, and either the angular Einstein radius, $\theta_{\rm E}$, or microlensing parallax, $\pi_{\rm E}$. Moreover, the lens flux is also important to confirm the physical parameters derived from $\theta_{\rm E}$ and $\pi_{\rm E}$.

2.3 Practical Application

The microlensing events are observed as a gradual increase of the brightness, followed by a gradual darkening to its original brightness. The microlensing phenomenon is very rare ($\sim 10^{-6}$ for a given bulge star) and the timescale of the planetary signal is very short (typically a few days for a Jupiter mass planet). Therefore, the wide field of view (FOV) and high cadence observations are required for microlensing.

2.3.1 Alert and Follow-Up

The strategy for the microlensing observations is first proposed by Gould & Loeb (1992). Their strategy consists of two steps. First, the wide FOV observations are conducted a few times per day or less and monitor the millions of bulge stars. Then, the transient alerts will be issued when the microlensing candidates are found. Second, the narrow FOV follow-up telescopes observe the alerted events many times per day. Note that this strategy assumed a $\sim 0.5\,\mathrm{deg}^2$ FOV CCD camera on 1.3m telescope for the survey observations. This strategy is still useful, especially for high-magnification events. The source trajectory passes very close to the center of the Einstein radius in such events (Figure 4). If there is a planet nearby the Einstein radius, the central caustic will appear near the lens host star. Therefore, high-magnification events are very sensitive to the planetary anomaly and the dense observations of this strategy can characterize the lens properties well.

2.3.2 Continuous Monitoring with Large Field-of-View Camera

The instruments of the recent microlensing survey telescopes have been upgraded and the new larger FOV cameras are available. These cameras have a few square degrees FOV with single pointing. This allows us to observe hundreds of millions of the bulge stars, dozens of times per day. Moreover, the number of survey telescopes that were built in different sites has increased. Thanks to these, many of the planetary and binary microlensing events are characterized by the current survey observations only (e.g. Koshimoto et al. 2014; Nagakane et al. 2017).

The MOA collaboration started such a large FOV and high-cadence microlensing survey observations toward the Galactic bulge for the first time in 2005. MOA conducts an efficient, nightly survey using a wide $2.2\,\mathrm{deg}^2$ FOV with a $10\mathrm{k} \times 8\mathrm{k}$ pixel mosaic CCD camera, MOA-cam3 (Sako et al., 2008), mounted on the 1.8 m MOA-II telescope at the Mt. John Observatory in New Zealand. About 600 microlensing events are alerted by MOA during the season when the Galactic bulge is observable.

In 2010, the OGLE collaboration also started the microlensing survey using a $1.4\,\mathrm{deg}^2$ FOV camera, OGLE-IV (Udalski et al., 2015), mounted on the 1.3 m Warsaw telescope located at Las Campanas Observatory in Chile. They alert ~ 2000 microlensing events in a year.

The Wise team had conducted the microlensing survey from 2010, using a $1.0\,\mathrm{deg}^2$ mosaic CCD camera mounted on the 1.0 m Wise telescope in Israel (Shvartzvald, & Maoz, 2012). They have already finished their survey observation in 2015.

The Korean Microlensing Telescope Network (KMTNet; Kim et al. 2016)

commenced their survey observations in 2015. They are using 4.0 deg^2 FOV with four 9k $\times$ 9k pixel mosaic CCD cameras mounted on the three 1.6 m wide-field optical telescopes at the Cerro-Tololo Inter-American Observatory (CTIO) in Chile, the South African Astronomical Observatory (SAAO) in South Africa, and the Siding Spring Observatory (SSO) in Australia. These three telescopes are located at three different continents in the Southern hemisphere. Therefore, the round-the-clock continuous monitoring of the microlensing events with $\sim$ 10 min cadence can be achieved. They also alert a few thousands of microlensing events per year.

2.3.3 High-Resolution Imaging by Follow-Up Observations

The actual observed flux from the microlensing event is derived as,

$$F(t) \equiv A(\boldsymbol{x}, t)\, F_{\rm S} + F_{\rm b} \tag{28}$$

where $A(\boldsymbol{x}, t)$ is the magnification as a function of time, $F_{\rm S}$ is the unmagnified flux from source star, and $F_{\rm b}$ is the blending flux. Here, $\boldsymbol{x}$ is the microlensing parameters that $\boldsymbol{x} = (t_0, t_{\rm E}, u_0)$ or $(t_0, t_{\rm E}, u_0, q, s, \alpha)$ for single or binary lens events, respectively. The blending flux $F_{\rm b}$ includes the flux from the possible sources of contamination (unrelated ambient stars, a companion to the source star, and a companion to the lens star) in addition to lens flux $F_{\rm L}$ explained in Section 2.2.4. If only the seeing limited ground-based observations (typically FWHM $\sim$ 1.5 arcsec) are conducted, the blending flux $F_{\rm b}$ is dominated by the flux from unrelated ambient stars in stellar crowded fields such as the Galactic bulge field. To reduce the flux from these contaminations, then to put a strong constraint to $F_{\rm L}$, a high angular resolution imaging (typically FWHM $<$ 0.2 arcsec) is required. The Adaptive Optics (AO) observation or the space-based observation can achieve this requirement.

If we observe the microlensing events with the high-resolution imaging when the lens and source stars are separated enough, we can detect the blending flux directly. Moreover, the relative proper motion μ_{rel} can be detected form this observation. The planetary microlensing event, OGLE-2005-BLG-169, is the event that the high-resolution imaging was conducted with *HST*/WFC3 and *Keck*/NIRC2 in 2011 and 2013, respectively (Bennett et al., 2015; Batista et al., 2015). They could provide tighter constraints to μ_{rel} from each follow-up observations. Moreover, the masses and distance of the planet and its host star were determined uniquely by combining the mass–distance relation from the lens brightness measurements and that from $\theta_{\rm E}$. They derived the lens host star mass as $0.69 \pm 0.02 M_\odot$ and $0.65 \pm 0.05 M_\odot$, independently. They assumed that the blending flux corresponds to the lens flux, actually this is not

true, but they could confirm that by comparing the two independent relative proper motion measurements in this case.

When the high-resolution imaging is carried out at the time that the lens and source stars are not elongate enough, the combined flux from the lens, source, and other blended stars can be observed. The magnification and the source flux are able to be obtained from light-curve fitting, the total flux from the lens and blend can be calculated by subtracting the source brightness from the combined flux. If the blending flux is detected significantly, it is possible to put constraints on the lens parameters by estimating the lens flux in consideration of the possible sources of contamination (Koshimoto et al., 2017, 2019). In some cases, the lens flux cannot be detected because the blending brightness is much fainter than the source brightness. Even so, we can put a tighter constraint from an upper limit of the lens flux to the lens parameters by the same method.

2.3.4 Near Infrared Surveys from Space

The future microlensing survey will be conducted by space-based telescopes. This space-based survey has a number of advantages over ground-based observations (Bennett, & Rhie, 2002). The *Wide Field InfraRed Survey Telescope* (*WFIRST*; Penny et al. 2019) is the next NASA astrophysics flagship mission, to follow the *James Webb Space Telescope* (*JWST*). The recent design of this space telescope (Cycle 7) is predicted that can detect $\sim$ 1400 exoplanets including $\sim$ 180 Earth-mass planets. *WFIRST* has a sensitivity for all the planets in the solar system except for the Mercury. On the other hand, the *Kepler* survey mission detected a large amount of close-in exoplanets. The combination of the *WFIRST* and the *Kepler* survey will be able to complete the planet distribution map on the separation–mass plane (Figure 9).

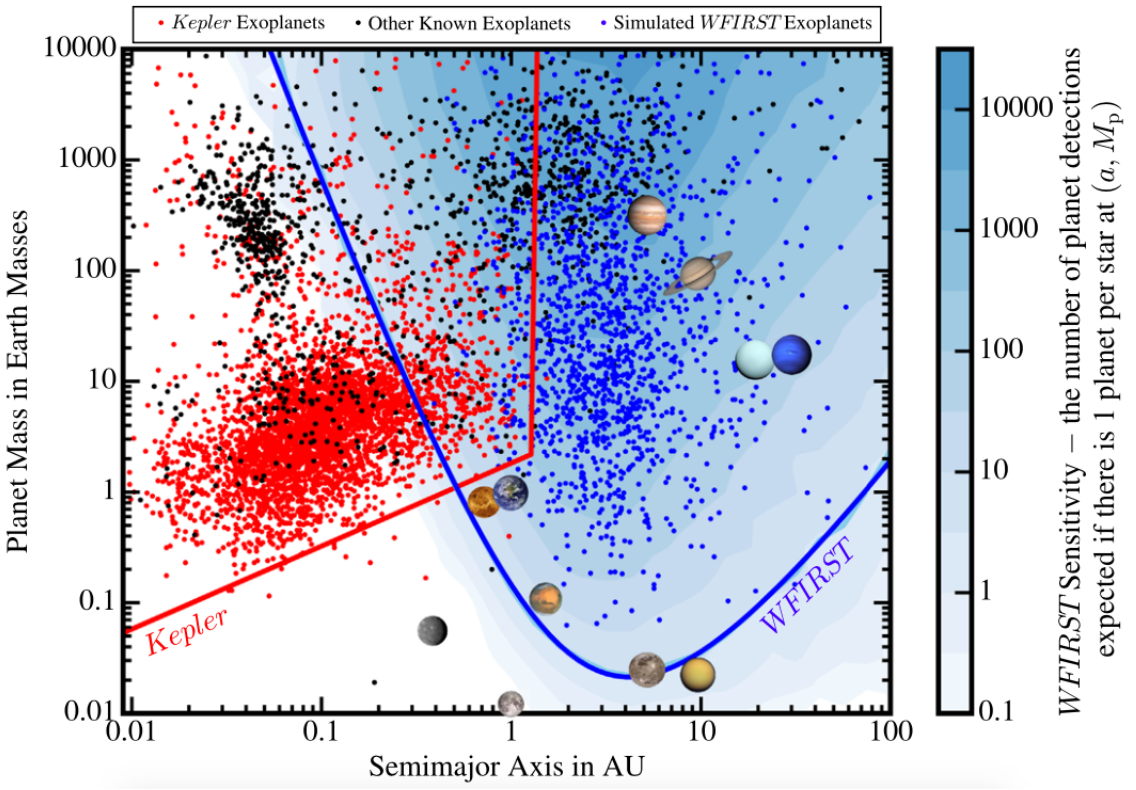

Figure 9: Sensitivity of *WFIRST* Cycle 7 design compared with that of *Kepler* (Penny et al., 2019). The number of WFIRST planet detections during the mission is shown as a blue contour. The red and blue lines show the planet detection limit of *Kepler* and a functional fit to the three-detection per mission, respectively. The solar system planets, the Moon, Ganymede, and Titan are shown by their images. Blue dots indicate that a simulated detection by the WFIRST microlensing survey. Red dots show the *Kepler* candidates and confirmed planets and black dots show the known exoplanets that are detected by other methods. (Figure 9 of "The Astrophysical Journal Supplement Series, Volume 241, Issue 1, article id. 3, 34 pp. (2019)": Reproduced by permission of Matthew T. Penny and the AAS.)

3 Analysis of OGLE-2015-BLG-1649

3.1 Observations

On 2015 July 18, HJD$-2450000 \equiv$ HJD$' = 7221$, the microlensing event OGLE-2015-BLG-1649 was discovered and alerted by the Optical Gravitational Lensing Experiment (OGLE; Udalski et al., 2015) Early Warning System (EWS). The source star of the event is located at $(\alpha, \delta)(2000) = (18^h04^m49\overset{s}{.}21,\ -32°37'58\overset{''}{.}90)$ which correspond to Galactic coordinates: $(l, b) = (-1\overset{°}{.}124, -5\overset{°}{.}422)$. The Microlensing Observations in Astrophysics (MOA; Bond et al., 2001; Sumi et al., 2003) collaboration independently found the event, which was named as MOA-2015-BLG-404, and alerted the discovery on 2015 July 30.

In the fourth phase of their survey, the OGLE collaboration is observing the Galactic bulge using the 1.3m Warsaw telescope located at Las Campanas Observatory in Chile (Udalski et al., 2015). The observations by OGLE were carried out in the I band and occasionally in the V band. In the following analysis, we use the V-band data only for independent color measurement of the source.

The MOA collaboration is also conducting a microlensing exoplanet search toward the Galactic bulge, using the 1.8m MOA-II telescope at Mt. John Observatory (MJO) in New Zealand. MOA conducts an efficient, nightly, high-cadence survey using a wide 2.2 deg^2 field of view (FOV) with a 10k $\times$ 8k pixel mosaic CCD camera, MOA-cam3 (Sako et al., 2008). The observations by MOA were mainly with a custom broad $R + I$-band filter called MOA-Red and with a V-band filter called MOA-V. MOA also conducted follow-up observations by using the 61cm Boller & Chivens (B&C) telescope at MJO with simultaneous g-, r-, i-band imaging.

The MOA collaboration noticed an anomaly, which appeared to be a caustic entry, on 2015 August 11, HJD$' = 7246.1$, and issued an alert, prompting follow-up observations. The RoboNet collaboration (Tsapras et al., 2009) conducted follow-up observations in the I band using the Las Cumbres Observatory Global Telescope (LCOGT) Network 1.0m telescopes sited at CTIO/Chile, SAAO/South Africa, and Siding Spring/Australia (Brown et al., 2013). In addition, the Microlensing Network for the Detection of Small Terrestrial Exoplanets (MiNDSTEp) conducted follow-up observations using the 1.54m Danish Telescope at the European Southern Observatory in La Silla, Chile (Dominik et al., 2010). The MiNDSTEp data were collected using an EMCCD camera with a long-pass filter $i_{\rm dk}$ resembling an extended SDSS-i + SDSS-z filter with a low-wavelength cutoff at 6500 Å (Skottfelt et al., 2015; Evans et al., 2016).

The light curves for these datasets are shown in Figure 10. The number of data points are also shown in Table 1.

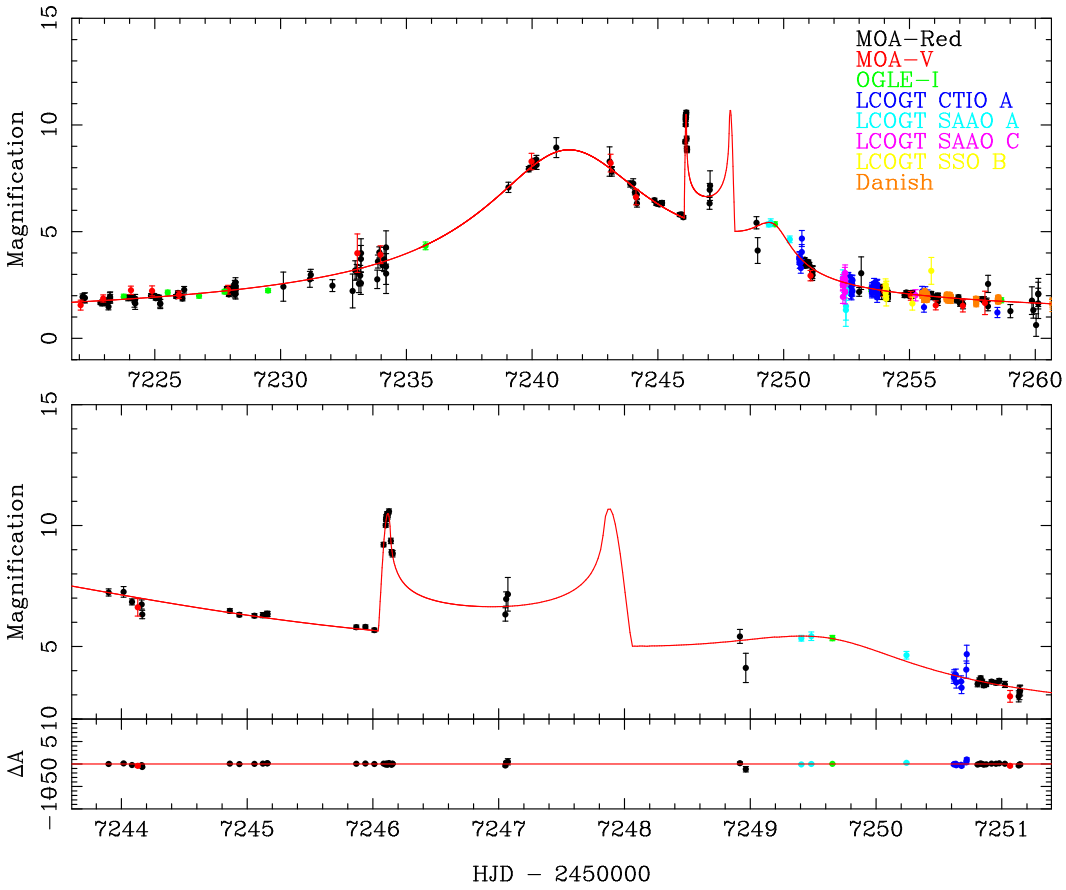

Figure 10: Light-curve data of event OGLE-2015-BLG-1649 with the best-fit model. The best-fit model is indicated by the red line. Bottom panel shows the details of the planetary signal and the residual from the best model. The data points taken by the B&C telescope are not shown for display purposes but models have been fitted to these data, as well as the data from all other sources.

Table 1: Data sets for OGLE-2015-BLG-1649 and the error correction parameters

Data set	Band	k	e_{min}	u_λ	Number of Data
MOA	$R+I$	1.236825	0	0.53645	2668
	V	1.031747	0.038893	0.6556	184
OGLE	I	1.270605	0	0.4953	870
B&C	g	0.728458	0	0.7276	125
	r	0.857322	0	0.6004	129
	i	0.760140	0	0.5152	125
LCOGT CTIO	I	1.031747	0	0.4953	56
LCOGT SAAO A	I	1.206830	0	0.4953	12
LCOGT SAAO C	I	1.128980	0	0.4953	15
LCOGT SSO B	I	1.454571	0	0.4953	10
Danish	$i_{\rm dk}$	0.491530	0	0.4543	86

We conducted high-resolution imaging observations to constrain the lens flux 40 days after detection of the anomaly using the Subaru telescope. We describe the details of the Subaru observations and the analysis in Section 3.5.

3.2 Data Reduction

The OGLE and MOA data are reduced with the OGLE Difference Image Analysis (DIA) photometry pipeline (Udalski, 2003) and MOA's implementation of a DIA pipeline (Bond et al., 2001), respectively. The RoboNet and MiNDSTEp data are reduced by using DanDIA (Bramich, 2008; Bramich et al., 2013). The DIA method has an advantage for the photometry of stars located in crowded fields such as the Galactic bulge field. It also produces better photometric light curves, because it is more efficient in dealing with the effect of blending compared to traditional point-spread function (PSF) photometry.

It is known that the nominal error bars calculated by the pipelines are incorrectly estimated in such crowded stellar fields for various reasons. We employ a standard empirical error bar normalization process (Yee et al., 2012) intended to estimate proper uncertainties for the lensing parameters in the light-curve modeling. This process, described below, does not affect the lensing parameters. We renormalize the photometric uncertainty using the formula

$$\sigma_i' = k\sqrt{\sigma_i^2 + e_{min}^2}, \tag{29}$$

in which σ_i' is the renormalized uncertainty in magnitude, while σ_i is uncertainty of the i-th original data point obtained from DIA. The variables k and e_{min} are renormalizing parameters. For preliminary modeling, we search for the best-fit lensing parameters using σ_i. We then construct a cumulative χ^2 distribution as a function of lensing magnification. The e_{min} value is chosen so that the slope of the distribution is unity. The k value is chosen so that $\chi^2/\mathrm{d.o.f.} \simeq 1$. In Table 1, we list the thus-derived error bar renormalization parameters.

3.3 Light-curve Modeling

The caustic entry of this event is well observed by MOA. (See Figure 10.) Unfortunately, while MOA was unable to observe the caustic exit, LCOGT data sample the critical caustic approach feature at $\mathrm{HJD}' = 7249.5$.

There are five microlensing parameters for a point-source point-lens (PSPL) model: the time of the closest lens–source approach t_0, the Einstein radius crossing timescale t_E, the impact parameter in units of the Einstein radius u_0, the source flux f_S, and the blend flux f_B. There are three more parameters for a point-source binary-lens model: the planet–host mass ratio q, the projected planet–host separation in units of the Einstein radius s and the angle between the trajectory of the source, and the planet–host axis α. In the case where the finite size of the source is considered (finite source effect), we include a source size in units of the Einstein radius $\rho \equiv \theta_*/\theta_\mathrm{E}$, where θ_* is the angular source radius, and θ_E is the angular Einstein radius of the lens. If microlensing parallax due to Earth's orbital motion is detected during the event, the north, $\pi_{\mathrm{E,N}}$ and east, $\pi_{\mathrm{E,E}}$, components of the microlensing parallax vector, $\boldsymbol{\pi}_\mathbf{E}$, are added. If effects from both finite source size and microlensing parallax are detected, we can uniquely determine the lens mass and the distance (Muraki et al., 2011; Street et al., 2019).

We conduct light-curve modeling using the Markov Chain Monte Carlo (MCMC) algorithm of Verde et al. (2003). For the computation of finite source magnification, we use the image-centered ray-shooting method (Bennett & Rhie, 1996; Bennett, 2010) implemented by Sumi et al. (2010). The overall shape of the lensing light curve is parameterized by (q, s, α). We conduct a grid search for these parameters, starting from 9680 grid points, while we search for the remaining parameters using a downhill simplex method. Subsequently, we search for the best model among the leading 100 candidate models from the initial grid search by allowing all parameters to vary. In microlensing event OGLE-2015-BLG-1649, we detect a finite source effect and use linear limb-darkening coefficients for a solar type star in the initial grid search and subsequent runs. Once a candidate model is found, we further refine it with updated linear limb-darkening coefficients based on source color to obtain the best-fit model. The stellar effective temperature T_eff, computed from the source color presented in Section 3.4, is $T_\mathrm{eff} = 5777 \pm 571$ K (González Hernández & Bonifacio, 2009). We assume $T_\mathrm{eff} \sim 5750$ K, a surface gravity of $\log g = 4.5$ (g is in a unit of $\mathrm{cm\,s^{-2}}$), the microturbulent velocity as $v_\mathrm{t} = 1\,\mathrm{km\,s^{-1}}$, and a metalicity of $\log[M/H] = 0$. We use the corresponding limb-darkening coefficients from the ATLAS stellar atmosphere models of Claret & Bloemen (2011), where the limb-darkening coefficients, u_λ, for these datasets are shown in Table 1.

In Table 2 and Figure 10, we present the lensing parameters and the model of the best-fit solution, respectively. In Figure 11, we also present the lens system configuration in which the source trajectory with respect to the binary-lens caustic is shown. We find that the best-fit model has a planetary mass ratio of $q = (7.2 \pm 0.2) \times 10^{-3}$ and a projected separation of $s = 0.902 \pm 0.001$.

Table 2: Best-fit parameters and 1σ errors

Parameter	Units	Value	Error (1σ)
t_0	HJD $-2450,000$	7241.170	0.033
$t_{\rm E}$	days	28.312	0.339
u_0	10^{-1}	1.146	0.028
q	10^{-3}	7.227	0.212
s	$\cdots$	0.902	0.001
α	radians	3.080	0.007
ρ	10^{-3}	1.265	0.055
θ_*	μas	0.703	0.062
$\theta_{\rm E}$	mas	0.556	0.055
$\mu_{\rm rel}$	mas yr^{-1}	7.138	0.674
d.o.f.	$\cdots$	4251	$\cdots$
χ^2	$\cdots$	4256.214	$\cdots$

Our analysis suggests that the proper motion of the source star causes it to cross the lensing system's caustic with the caustic entry and one crossing well sampled by the MOA data. Because the infinitesimally thin caustic effectively resolves the source star, inclusion of the finite source effect improves the fit by $\Delta\chi^2 = 597.3$. In contrast, the inclusion of the microlensing parallax effect improves the fit by only $\Delta\chi^2 = 5.4$, i.e., less than 2σ. We therefore adopt the best model, including the finite source effect while excluding parallax, in the subsequent analysis.

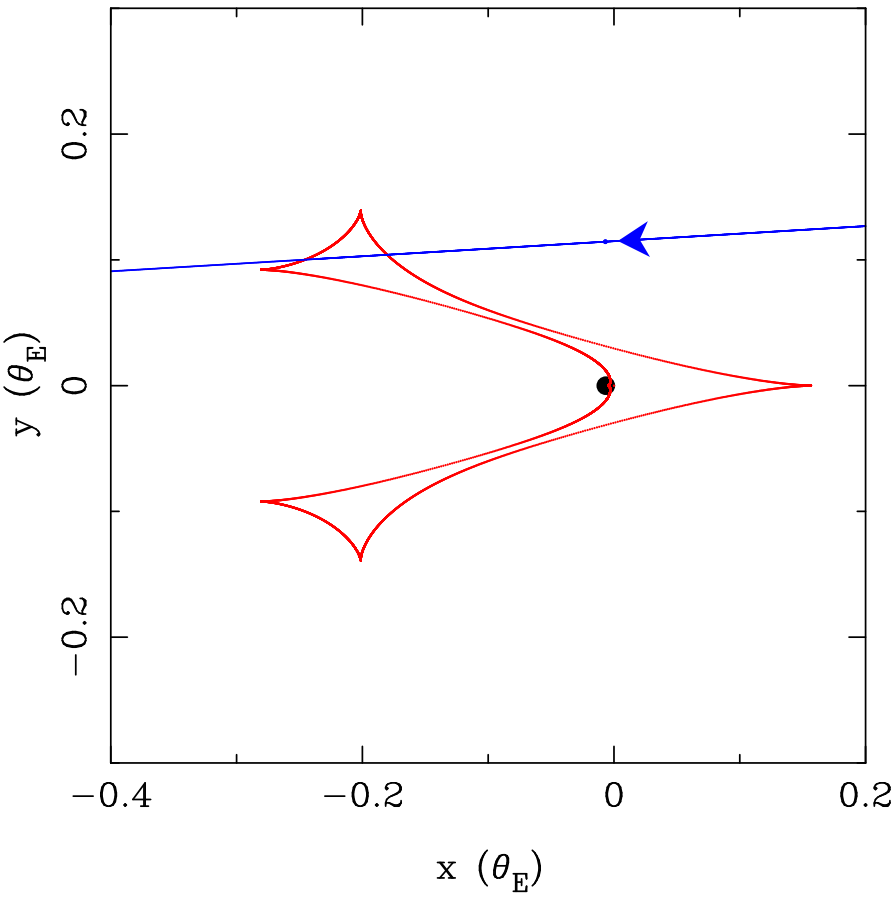

Figure 11: Caustic geometries for the best-fit model indicated by the red curve. The blue line shows the source trajectory with respect to the lens system. The blue circle indicates the source star size. The origin of the coordinate system corresponds to the barycenter of the lens system. The planet is located at (s, 0).

3.4 Color–Magnitude Diagram and Source Radius

In this section, we estimate the angular Einstein radius $\theta_{\rm E} = \theta_*/\rho$ from the combination of ρ and θ_*, where the normalized source radius is measured from the light-curve modeling and the angular source radius is estimated from the color and brightness of the source. We obtain the source color and magnitude by fitting the light curve to the MOA-Red band and MOA-V band data. Figure 12 shows the OGLE-III $(V-I, I)$ color–magnitude diagram (CMD) of stars within $2'$ around the source (Szymański et al., 2011). It also shows the deep CMD of Baade's window observed by the *Hubble Space Telescope* (*HST*; Holtzman et al., 1998). The *HST* CMD is aligned to the ground-based CMD considering the distance, reddening, and extinction to the OGLE-2015-BLG-1649 field by using red clump giants (RCG) as standard candles (Bennett et al., 2008). We convert the best fit MOA-Red and MOA-V source magnitude to the standard Cousins I and Johnson V magnitudes by cross-referencing stars in the MOA field with stars in the OGLE-III photometry map (Szymański et al., 2011) within $2'$ of the event. We find the source color and magnitude to be $(V-I, I)_{\rm S,OGLE} = (1.51\pm0.03, 19.43\pm0.02)$. We independently measure the source color by using OGLE-I and V light curves and we found $(V-I)_{\rm S,OGLE} = 1.52 \pm 0.09$, which is consistent with above value. We use $(V-I)_{\rm S,OGLE} = 1.51 \pm 0.03$ in the following analysis. The centroid of RCG color and magnitude in the CMD are $(V-I, I)_{\rm RCG} = (1.88\pm0.03, 15.73\pm0.06)$ as shown in Figure 12. Comparing these values to the expected extinction-free RCG color and magnitude at this field of $(V-I, I)_{\rm RCG,0} = (1.06\pm0.07, 14.51\pm0.04)$ (Bensby et al., 2013; Nataf et al., 2013), we get the reddening and extinction to the source of $(E(V-I), A_I) = (0.82 \pm 0.08, 1.22 \pm 0.07)$. Therefore, we estimate the extinction-free source color and magnitude as $(V-I, I)_{\rm S,0} = (0.69 \pm 0.08, 18.21 \pm 0.07)$. By using the empirical formula, $\log(2\theta_*) = 0.5014 + 0.4197(V-I) - 0.2I$ (Boyajian et al., 2014; Fukui et al., 2015), we estimate the angular source radius to be

$$\theta_* = 0.70 \pm 0.06 \ \mu{\rm as}. \tag{30}$$

From this θ_* and other fitting parameters, we calculate the angular Einstein radius $\theta_{\rm E}$ and the lens–source relative proper motion $\mu_{\rm rel} = \theta_{\rm E}/t_{\rm E}$, as follows,

$$\theta_{\rm E} = 0.57 \pm 0.06 \ {\rm mas} \tag{31}$$

$$\mu_{\rm rel} = 7.14 \pm 0.67 \ {\rm mas\ yr^{-1}}. \tag{32}$$

$$\tag{33}$$

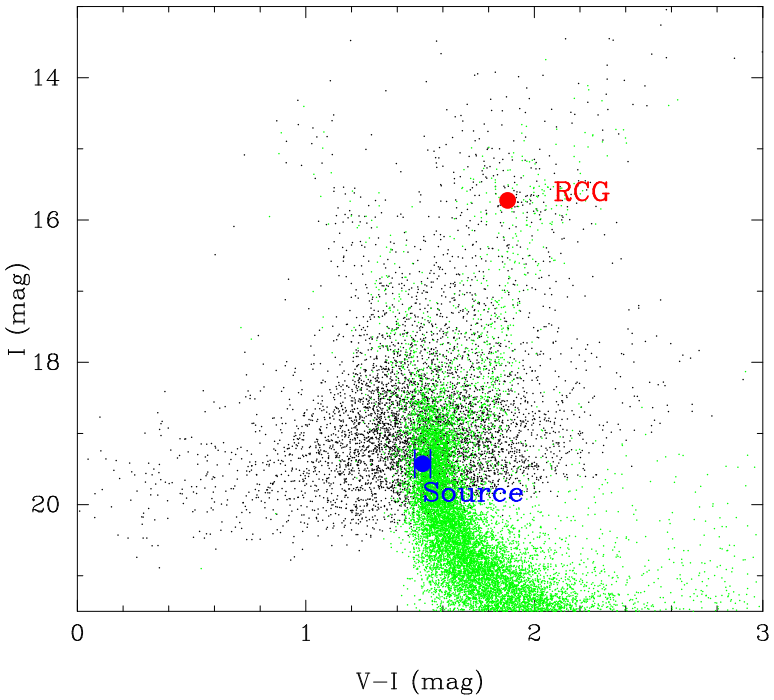

Figure 12: Color–magnitude Diagram (CMD) of OGLE-III stars within 2′ of OGLE-2015-BLG-1649 (black dots). The green dots show the HST CMD (Holtzman et al., 1998). The red point indicates the centroid of the red clump giants, and the blue point indicates the source color and magnitude.

3.5 Infrared Camera and Spectrograph AO Images

We conducted high-resolution imaging follow-up observations of OGLE-2015-BLG-1649 using the Infrared Camera and Spectrograph (IRCS; Kobayashi et al., 2000) with the AOs system AO188 (Hayano et al., 2010) mounted on the 8.2m Subaru Telescope on 2015 September 18 at 5:17 – 6:05 UT ($\mathrm{HJD}' = 7283.7$). We employed the high-resolution mode of IRCS, which delivers a pixel scale of 20.6 mas/pixel and a $21'' \times 21''$ FOV. For AO correction, we use a bright star located close to the source star. We obtained 15 exposures in the H and K' bands with 24 s exposures with a five-point dithering and 15 J band with 30 s exposures with a five-point dithering (Figure 13). The AO-corrected seeing was $0\farcs37$, $0\farcs22$, and $0\farcs19$ for the J, H, and K' images, respectively.

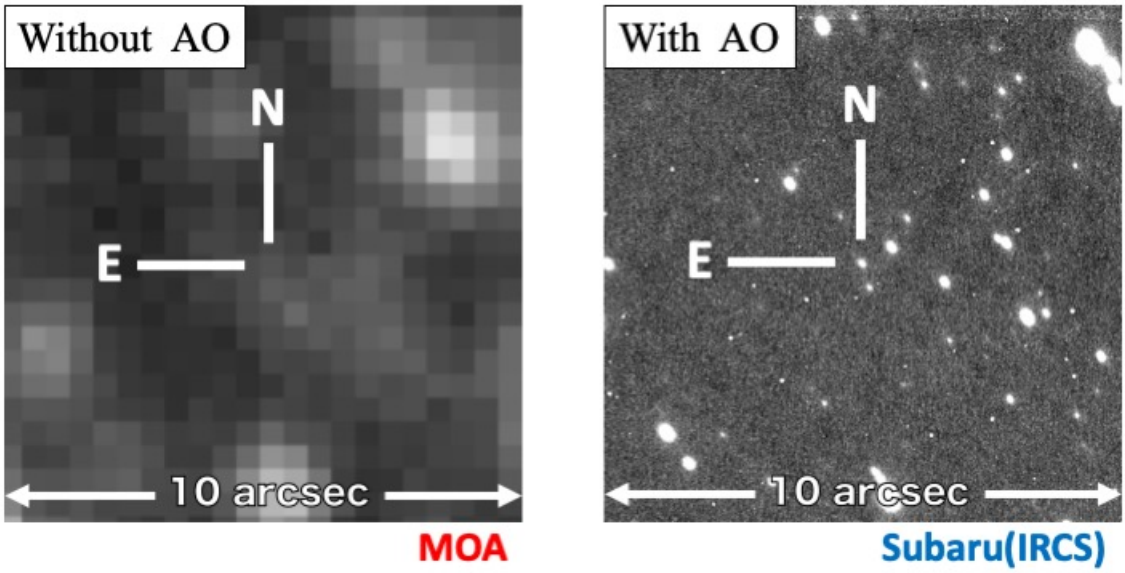

Figure 13: (Left) Image without AO taken by MOA-II telescope. (Right) High-resolution image with AO taken by Subaru/IRCS. OGLE-2015-BLG-1649 is located at the center of cross heirs in each image.

Image reductions are carried out in a standard manner, including flat-fielding and sky-subtraction. We then combine all single-exposure images to form deep stacked images in each passband. The stacked images are further aligned with the Visible and Infrared Survey Telescope for Astronomy (VISTA) Variables in the Via Lactea (VVV; Minniti et al., 2010) images for astrometric calibration. We estimate the flux

of OGLE-2015-BLG-1649 using aperture photometry. We conduct calibration in a photometric ladder manner: we first calibrate the photometry of IRCS stacked images against the VVV data, and then scale to the Two Micron All Sky Survey (2MASS; Skrutskie et al., 2006) photometric system (Figure 14). We find that the brightness of the event at the time of the AO observation is

$$J_{target} = 18.467 \pm 0.189, \quad (34)$$

$$H_{target} = 17.870 \pm 0.217, \quad (35)$$

$$K'_{target} = 17.667 \pm 0.127. \quad (36)$$

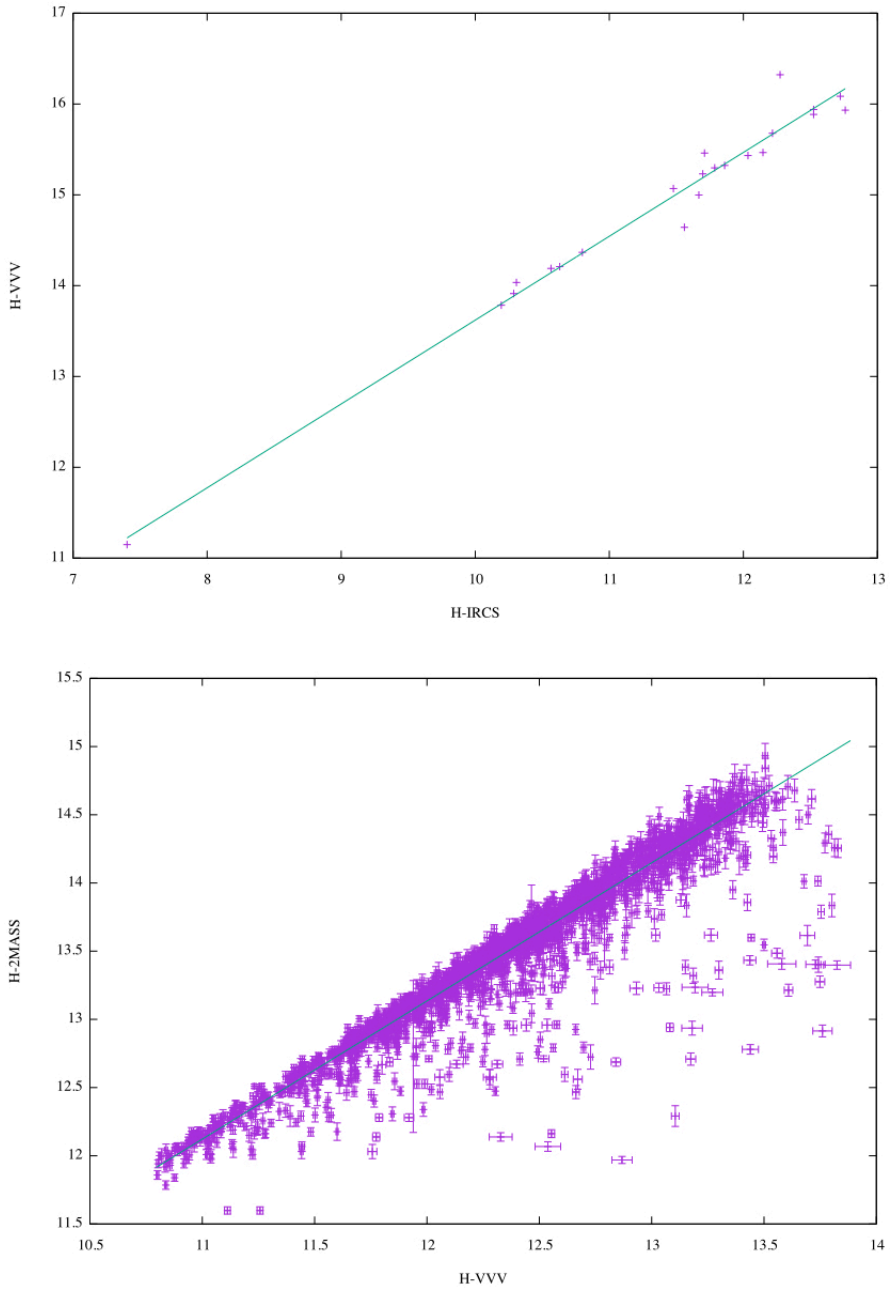

Figure 14: (Top) H-band magnitude of VVV versus H-band magnitude of IRCS. (Bottom) H-band magnitude of 2MASS versus H-band magnitude of VVV. The solid lines are the polynomial fit for observed data.

3.6 Excess Flux

The measured angular Einstein radius provides a mass–distance relation, i.e., $M = (4G/c^2)^{-1}\theta_{\rm E}^2 D_{rel}$. A second mass–distance relation may be estimated in the case where the lens flux is detected. If both relations can be measured, the lens mass can be uniquely determined. High-resolution imaging with IRCS/Subaru gives us the combined flux from the lens, source, and other blended stars. If we can obtain the source flux from light-curve fitting, the total flux from the lens and blend can be calculated by subtracting the source brightness from the combined flux (equation 34-36). We do not have light-curve data in the J, H and K bands. Therefore, we derive the source magnitude in the H band as $H_{\rm S,0} = 17.57 \pm 0.12$ by converting $(V-I, I)_{\rm S,0} = (0.69 \pm 0.08, 18.21 \pm 0.07)$ with the color–color relation by Kenyon & Hartmann (1995). We use the CMD of VVV to derive the extinction value in the H band, A_H. We subsequently compare the centroid of RCG on the CMD and the intrinsic position of RCG derived by Nataf et al. (2016) resulting in an extinction value of $A_H = 0.41 \pm 0.12$.

The magnification at the time of the Subaru observation is $A = 1.128$ according to the best-fit model. The apparent H-band magnitude of the source at the time is expected to be $H_{\rm S,AOtime} = 17.84 \pm 0.15$ in the 2MASS system (Janczak et al., 2010; Carpenter, 2001). This suggests that the H-band flux observed by Subaru mainly comes from the slightly magnified source. We can place the 1σ upper limit of the excess brightness of $H_{\rm excess} > 19.11$. Using a similar process, we obtain 1σ upper limits of excess brightness $J_{\rm excess} > 20.18$ and $K_{\rm excess} > 19.21$.

3.7 Lens Properties through Bayesian Analysis

To estimate the properties of the lens system, we consider the probability of possible sources of contamination (unrelated ambient stars, a companion to the source star, and a companion to the lens star) in the estimated excess H-band flux, $H_{\rm excess}$ (Batista et al., 2014; Fukui et al., 2015; Koshimoto et al., 2017). Following the method of Koshimoto et al. (2017), we determine the posterior probability distributions of these sources for the origin of the excess flux. We use the Galactic model of Han & Gould (1995) as our prior distribution and the measured $\theta_{\rm E}$ and $t_{\rm E}$ to constrain the posterior probability distributions of lens parameters. Figure 15 shows the posterior probability distributions of the lens mass $M_{\rm L}$, the distance to the lens system $D_{\rm L}$, total magnitude of contamination $H_{\rm excess}$, magnitude of the lens star $H_{\rm L}$, magnitude of ambient star $H_{\rm amb}$, magnitude of source companion $H_{\rm SC}$, and magnitude of lens companion $H_{\rm LC}$.

With the upper limit on lens brightness, we can make the posterior probability distribution much narrower. We use the probability distributions in Figure 15 to extract combinations of the parameters that satisfy the 1σ upper limit of $H_{\rm excess} > 19.11$. Figure 16 shows the posterior probability distributions with the additional constraint of the excess brightness limit. Table 3 shows the median and 1σ range of $H_{\rm L}$, $M_{\rm L}$, $D_{\rm L}$, the values of the planet mass $M_{\rm p}$, the projected separation $a_\perp$ and the 3D star–planet separation $a_{\rm 3d}$ for the posterior probability distribution with and without the excess brightness limit. The intrinsic orbital separation $a_{\rm 3d}$ is estimated assuming a uniform orientation of the planets, i.e., $a_{\rm 3d} = \sqrt{(3/2)}\, a_\perp$. More details can be found in Koshimoto et al. (2017).

Table 3: Lens properties calculated from the posterior probability distribution with and without the Subaru AO data

		Without the Subaru Data		With the Subaru Data	
Parameter	Units	Median	1σ Range	Median	1σ Range
$H_{\rm L}$	mag	19.68	$18.07 - 20.79$	20.52	$19.85 - 21.25$
$M_{\rm L}$	$M_\odot$	0.56	$0.26 - 0.87$	0.34	$0.15 - 0.53$
$M_{\rm p}$	$M_{\rm Jup}$	4.27	$1.96 - 6.61$	2.54	$1.15 - 4.02$
$D_{\rm L}$	kpc	5.20	$3.50 - 6.34$	4.23	$2.59 - 5.74$
$a_\perp$	au	2.57	$1.77 - 3.14$	2.07	$1.30 - 2.72$
$a_{\rm 3d}$	au	3.13	$2.04 - 4.89$	2.56	$1.56 - 4.03$

While our Bayesian treatment of these data do not exclude the probability of a

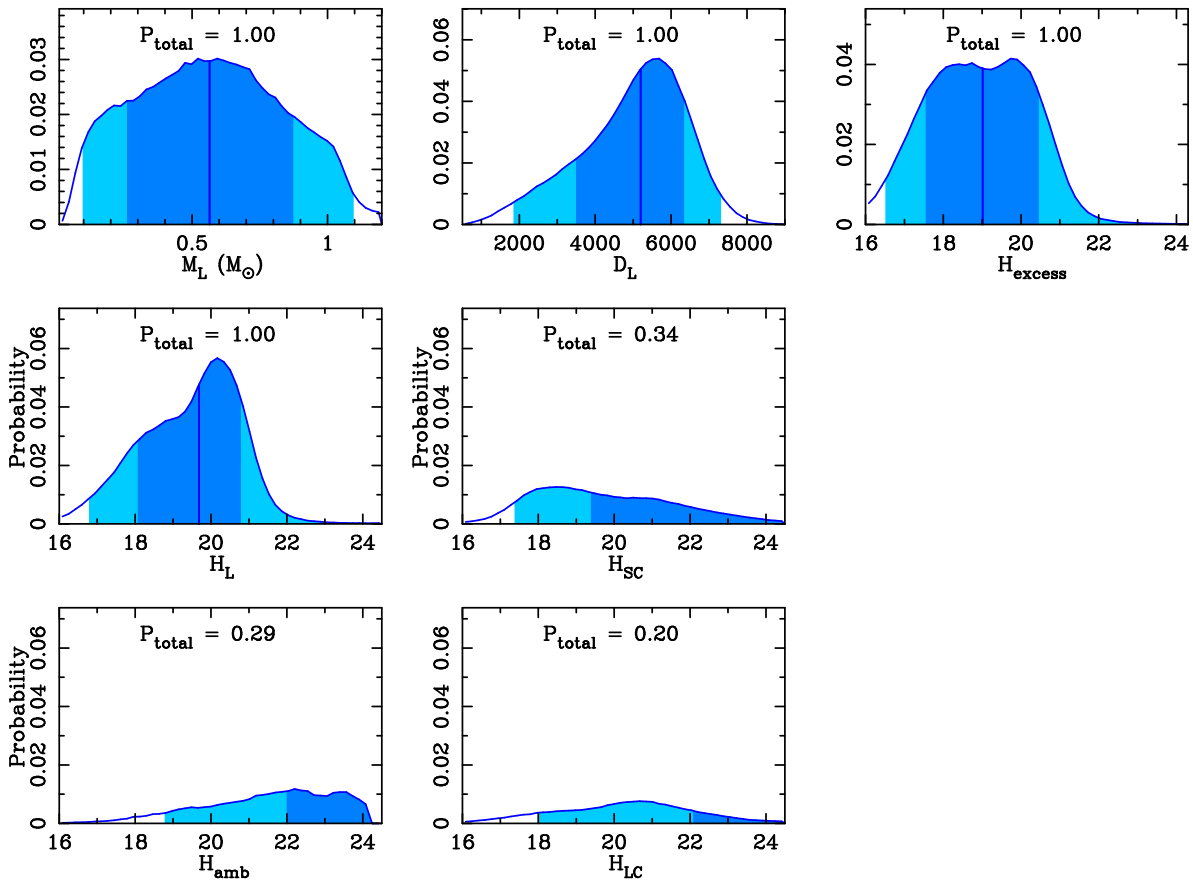

Figure 15: Posterior probability distributions of the lens mass $M_{\rm L}$, the distance to the lens system $D_{\rm L}$, total magnitude of contamination $H_{\rm excess}$, magnitude of the lens star $H_{\rm L}$, magnitude of source companion $H_{\rm SC}$, magnitude of ambient star $H_{\rm amb}$, and magnitude of lens companion $H_{\rm LC}$. The dark and light blue regions indicate the 68% and 95% confidence intervals, respectively. The vertical blue lines indicate the median values of each of the distributions. These distributions have not been constrained by the excess brightness limit.

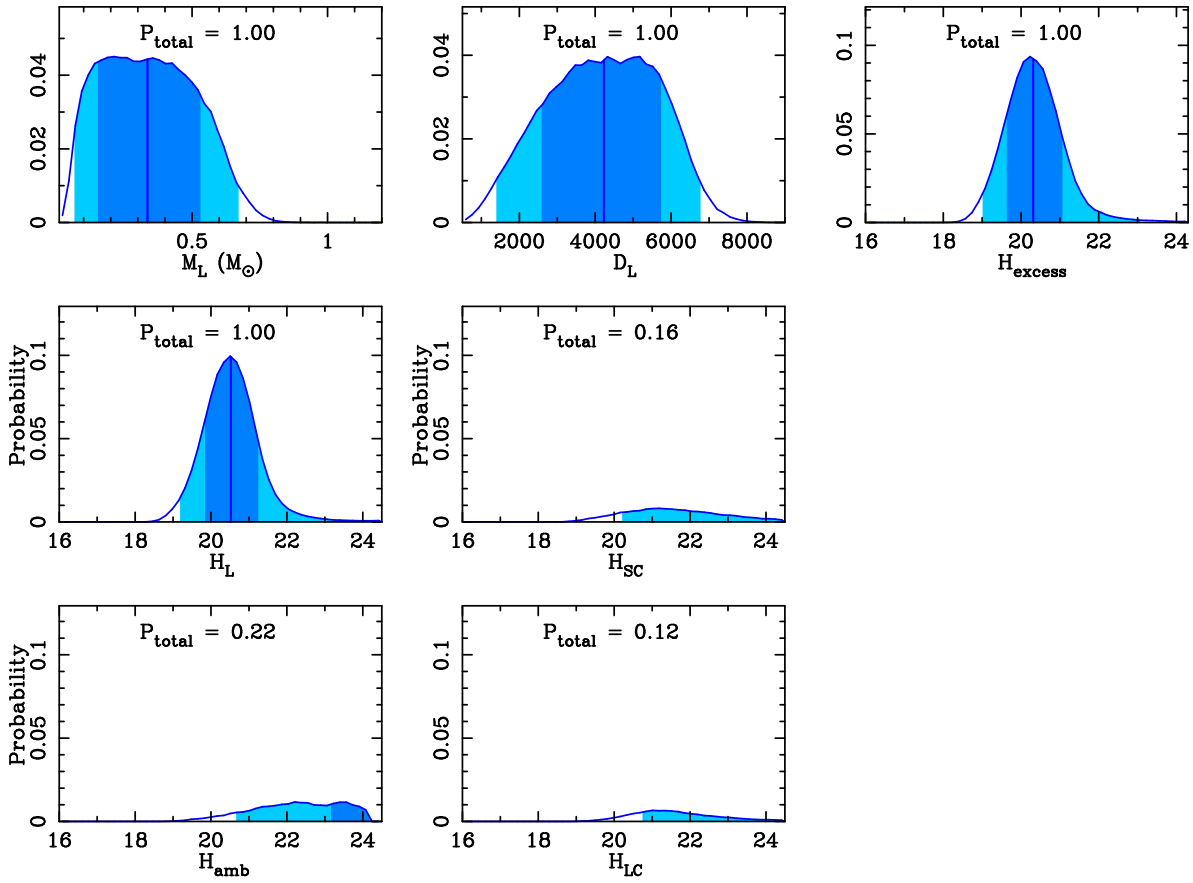

Figure 16: Posterior probability distributions narrowed by the additional constraint of the excess brightness limit. The panel in the upper left suggests that the host star is almost certainly less massive than a G dwarf.

G-dwarf host (Figure 15, upper left), examination of the posterior distribution obtained with the constraint of the excess brightness limit (Figure 16) allows us to assert that the host star is almost certainly less massive. These results are consistent with similarly derived distributions for the J- and K bands.

The posterior distribution with an excess brightness limit shows that the most likely lens brightness is $H_{\rm L} = 20.52$. Since the uncertainty of the source star magnitude in the H band is relatively large, we would have failed to detect the excess flux even if the seeing conditions were better during the Subaru observations. Consequently, the lens and source stars must be spatially resolved to measure the H-band lens flux. For this reason, this event is one of the high-priority candidates for follow-up observations with high-resolution imaging because of the high relative proper motion and relative faintness of the source star.

4 Discussion and Conclusion

We have here described the discovery of a planetary system, OGLE-2015-BLG-1649L, composed of a giant planet with $M_{\rm p} = 2.5^{+1.5}_{-1.4}\ M_{\rm Jup}$ and an M or late K-dwarf host with $M_{\rm L} = 0.34 \pm 0.19\ M_{\odot}$. Our analysis suggests that it is likely that the brightness values of possible sources of contamination are, in the aggregate, fainter than the brightness of the lens star. This suggests that the color-dependent centroid shift is likely to be caused by the lens itself. We estimate that the color-dependent centroid shift for this event will be $dx \sim 2.1$ mas in 2019 using the relation $dx = dt \times (f_H - f_V) \times \mu_{\rm rel}$, in which $f_H = 0.09$ and $f_V = 0.01$ are the fraction of the lens + source flux that is due to the lens in the H and V bands, respectively (Bennett et al., 2007; Hirao et al., 2016). Although our Subaru AO observations were carried out when the source star was still magnified, we can yet obtain the source magnitude in the H band directly if additional Subaru observations are conducted in the near future. Considering the high relative proper motion, image elongation could be also measured with high-resolution observations in a few years time (Bhattacharya et al., 2018). For these reasons, this planetary microlensing event should be one of the highest priorities for future observation using a high-resolution instrument.

To derive the cold planet frequency as a function of physical parameters, such as, host star mass, Galactocentric distance, and planet mass function, it is manifestly desirable to use planet mass data that has been tightly constrained. IRCS AO observations permitted an estimate of an upper limit on the excess flux. This, in turn, provided a significantly tighter constraint on the lens flux than using the blending flux alone. While the planetary parameters we have estimated here depend greatly on the prior distribution, our Bayesian analysis permits us exclude lens models in which the host star is a G dwarf or a more massive star with relatively high credibility. In this study, we successfully demonstrated that we can reduce the uncertainty in host star mass using an upper limit on the lens flux from AO images. Collecting AO imaged microlensing event data will be important for studying the planet mass function before the Wide Field Infrared Survey Telescope (WFIRST; Penny et al., 2019) era.

Finally, according to the standard core accretion model (Safronov, 1972; Hayashi et al., 1985; Lissauer, 1993), gas giant planets should seldom form around low-mass stars. By contrast, the disk instability model (Boss, 1997) suggests no such restriction. Taken together with other gas giant/low-mass dwarf planetary systems that have been discovered (e.g., Koshimoto et al., 2017), OGLE-2015-BLG-1649Lb poses a challenge the former and appears to support the latter.

Appendix A MOA-2012-BLG-505Lb: A Super-Earth-mass Planet That Probably Resides in the Galactic Bulge

A.1 Introduction

Since the first discovery of an exoplanet orbiting a main-sequence star (Mayor & Queloz, 1995), more than 3000 exoplanets have been discovered. Most of these were discovered by the radial velocity method (Butler et al., 2006) and the transit method (Borucki et al., 2011). Although these methods have a higher sensitivity to planets with higher masses and closer orbits in general, their sensitivities are evolving to allow the discovery of planets of lower mass at wider orbits. The Kepler satellite revolutionized our understanding of the exoplanet distribution by detecting many small planets down to Earth-radius planets with semi major axes of less than 1 au. However, the population of low-mass planets with separations of a few astronomical units are less understood.

Exoplanet searches using gravitational microlensing were first proposed by Mao & Paczyński (1991). If a background source star is closely aligned with a foreground lens star, the gravity of the lens bends the light from the source star to create unresolvable images of the source, yielding an apparent magnification of the source star brightness. If the lens star has a planetary companion and it lies close to one of the source images, the gravity of the planet perturbs the observed light curve. Microlensing is uniquely sensitive to exoplanets at orbit radii $1 - 6$au, just outside of the snow-line (Ida & Lin, 2004b; Laughlin et al., 2004; Kennedy et al., 2006) with masses down to Earth-mass planets. Contrary to the other planet detection methods mentioned above, microlensing does not rely on any light from the host star. Microlensing is also sensitive to low-mass planets (Bennett & Rhie, 1996) orbiting the faint and/or distant stars, like late-M-dwarfs, the most common stars in our Galaxy.

Since the first discovery of exoplanets by microlensing (Bond et al., 2004), about 50 planetary microlensing events have been found. Many microlensing planets have been discovered in high-magnification ($A \gtrsim 100$) events. Although the high-magnification events are rare, the events are very sensitive to planets (Griest & Safizadeh, 1998; Rhie et al., 2000; Rattenbury et al., 2002). Therefore, we issue alerts for high-magnification events to encourage follow-up observations to detect and characterize planetary anomalies in the light curves. We report the discovery of a planetary system in the Galactic bulge in the high amplification microlensing event MOA-2012-BLG-505.

We describe the observations and the data set of this event in Section A.2. The light-curve modeling is described in Section A.3. Section A.4 presents the data calibration and the source star radius estimate. In Section A.5, we present a Bayesian analysis, which is used to estimate the physical parameters of the lens system. Finally, our discussion and conclusions are given in Section A.6.

A.2 Observation and Data

The Microlensing Observations in Astrophysics (MOA; Bond et al., 2001; Sumi et al., 2003) collaboration is conducting a microlensing exoplanet search toward the Galactic bulge using the 1.8m MOA-II telescope at Mt. John University Observatory (MJUO) in New Zealand. Thanks to the wide field of view (FOV) of 2.2 $\deg^2$ with 10k $\times$ 8k pixel mosaic CCD-camera, MOA-cam3 (Sako et al., 2008), we conduct a high cadence survey observations depending on the field. The observations are carried out mainly with a custom broad $R + I$ band filter, called MOA-Red.

On 2012 July 27, UT 17:48, the microlensing event MOA-2012-BLG-505 was detected and alerted by MOA at $(\alpha, \delta)(2000) = (17^h52^m34^s.34, -32°02'24''.33)$ corresponding to Galactic coordinates: $(l, b) = (-1.892°, -2.881°)$. This event was alerted at HJD$-2450000 = 6136.24$ and, because the event was very short and fast-rising, the alert was issued after peak magnification and when the planetary signal at the peak was already over. Therefore, no follow-up observation was conducted on this event by other groups. Fortunately, this event occurred in one of the fields with the highest cadence observation of 15 minutes. Thus we could detect a short subtle planetary signature by MOA data alone. Figure 17 shows the observed light curve.

The MOA data were reduced with MOA's implementation of a Difference Image Analysis (DIA) pipeline (Bond et al., 2001). This method has the advantage for detecting objects whose brightness changed in the stellar crowded fields like those in the Galactic bulge by subtracting good-quality reference images from each of the observed images. It also produces better photometric light curves, avoiding the effect of blending stars compared to traditional PSF photometry. Moreover, our pipeline is designed to be sensitive to those events whose source star is fainter and not resolved in the reference image, but magnified brighter than observational limiting magnitude by the microlensing, as in this event.

It is known that the nominal error bars calculated by the pipeline are misestimated in such stellar crowded fields due to various reasons. We empirically renormalized the errors by using the standard method (Yee et al., 2012) as follows. Note that this renormalization is intended to produce proper errors of the parameters in the

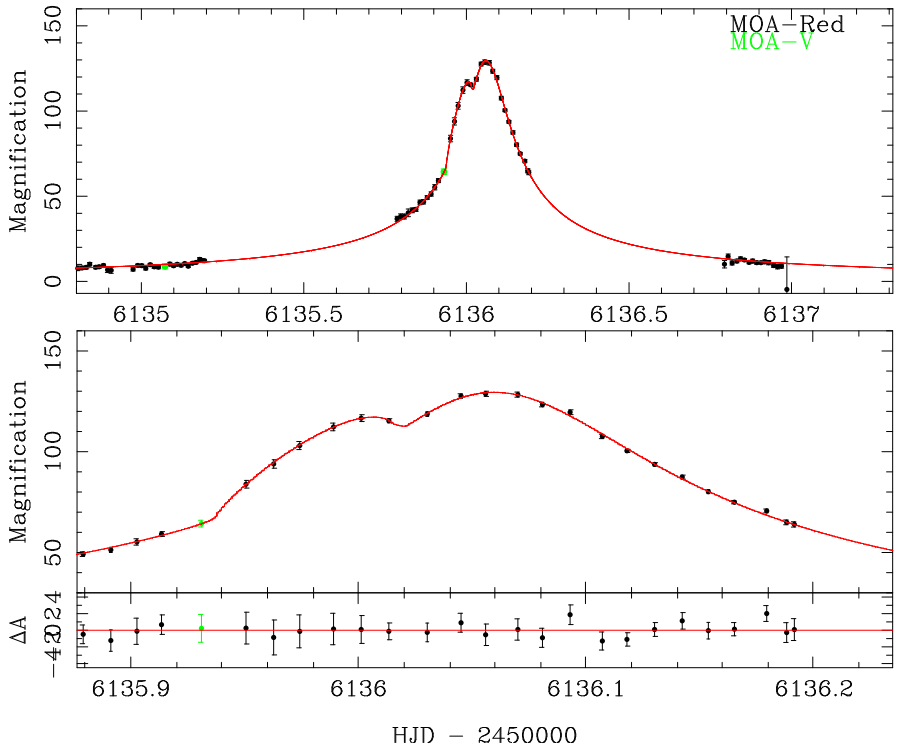

Figure 17: The light curve of event MOA-2012-BLG-505 with data from MOA-Red (black) and MOA-V (Green). The best-fit model is indicated by the red line. Middle and bottom panels show the detail of planetary signal and the residual from the best model respectively.

light-curve modeling, and we made sure that the fitting results do not depend on this renormalization. We renormalized by using the formula,

$$\sigma_i' = k\sqrt{\sigma_i^2 + e_{\rm min}^2} \tag{37}$$

where σ_i' is the ith renormalized error, σ_i is the ith error obtained from DIA, and k and $e_{\rm min}$ are the renormalizing parameters.

At first, we searched the preliminary best-fit model by using light curves with original errors. Then we sort the data points by magnification and make a cumulative χ^2 distribution. The $e_{\rm min}$ value is chosen such that the slope of the distribution is 1. The k value is chosen such that $\chi^2/{\rm dof} \simeq 1$. As a result, we obtained $e_{\rm min} = 0$ and $k = 1.351988$ for MOA-Red, $e_{\rm min} = 0$ and $k = 0.932111$ for MOA-V.

A.3 Light-curve Models

There are five microlensing parameters for a point-source point-lens (PSPL) model: the time of lens–source closest approach t_0, the Einstein timescale $t_{\rm E}$, the minimum impact parameter in units of the Einstein radius u_0, the source flux $f_{\rm S}$, and the blend flux $f_{\rm B}$. There are three more parameters for a point-source binary (planetary)-lens model: the planet–host mass ratio q, the planet–host separation in units of the Einstein radius s, the angle between the trajectory of the source and the planet–host axis α. Moreover, if the finite size of the source is considered (finite source effect), we need the source size in units of the Einstein radius $\rho \equiv \theta_*/\theta_{\rm E}$, where θ_* is the angular source radius and $\theta_{\rm E}$ is the angular Einstein radius. If the effect of Earth's orbital motion during the event, called the microlensing parallax effect, is significant, the north and east components of the microlensing parallax vector $\pi_{\rm E,N}$ and $\pi_{\rm E,E}$ are added, respectively. If both the finite source effect and the microlensing parallax effect are detected, we can determine the lens mass and the distance directly (Muraki et al., 2011).

To fit the microlensing parameters, we used the Markov Chain Monte Carlo (MCMC) algorithm (Verde et al., 2003) and the Sumi et al. (2010) implementation of the image centered ray-shooting method (Bennett & Rhie, 1996; Bennett, 2010). Three microlensing parameters, (q, s, α), feature the anomaly shape well, thus we first conduct a grid search of 9680 fixed grid points of these parameters leaving the other parameters free. We used 11 values for $\log q$ over the range $\log q \in [-4, 0]$, 22 values for $\log s$ in the range $\log s \in [-0.5, 0.55]$ and 40 values of α in the range $\alpha \in [0, 2\pi]$. Then we searched for the best model by refining the best 100 models from the initial grid search with all parameters free. In this event, we detected a finite source effect.

To obtain the value of ρ properly, we included linear limb-darkening. The stellar effective temperature $T_{\rm eff}$ computed from the source color presented in Section A.4 is $T_{\rm eff} \sim 6213\,{\rm K}$ (González Hernández & Bonifacio, 2009). We assumed $T_{\rm eff} \sim 6250\,{\rm K}$, a surface gravity of $\log g = 4.5\,{\rm cm\,s^{-2}}$, the microturbulent velocity as $v_{\rm t} = 0\,{\rm km\,s^{-1}}$, and a metallicity of $\log[M/H] = 0$. We used the corresponding limb-darkening coefficient from the ATLAS stellar atmosphere models of Claret (2000), and found the coefficient for MOA-Red is $u = 0.52845$ by taking the mean of the R- and I-band values. We also determined the coefficient for MOA-V is $u = 0.6413$.

Because the peak magnification of the event is $A_{\rm max} \sim 100$, the event is very sensitive to the planetary perturbations. Figure 17 shows the best-fit model and the light curve of this event. Table 4 presents the best-fit model parameters. We found that the best-fit model with planetary mass ratio of $q = 2 \times 10^{-4}$ reproduces the asymmetric feature at the peak of light curve in this event. Comparing to the single lens model, the best planetary model improves χ^2 by $\Delta\chi^2 \sim 227$. Therefore, the planetary signal is detected significantly.

The inclusion of the finite source effect improves the fit by $\Delta\chi^2 = 17.1$, i.e., larger than 4σ. The comparison between the model with and without the finite source is shown in Figure 18. One can see that the model with the finite source fits the data better around the event peak. Thus, we include the finite source effect in the following analysis. Because the source trajectory of the best-fit model crosses only the central caustic as is common in high-magnification events, there is the well known close–wide degeneracy. The microlensing parameters are almost the same except for the separations. The models with $s < 1$ and $s > 1$ are called the close and wide models, respectively. In this event, the shapes of the central caustics for both close and wide models are fairly similar, as shown in Figure 19. The χ^2 difference between these models is only $\Delta\chi^2 = 0.019$; therefore, we cannot distinguish them.

We did not detect the microlensing parallax effect in this event. This is as expected because the event is short with a timescale of ~ 10 days (Gould, 1992; Gaudi, 2012).

We also found a model with a stellar mass ratio of $q \sim 6.7 \times 10^{-2}$, which is the second preferred model with $\Delta\chi^2 \sim 32$ compared to the best close–wide planetary models above. Although the best planetary models have significant $\Delta\chi^2$ compared to the best single lens model, the distinction of these models against stellar binary models is marginal because of relatively subtle anomaly features. To confirm that our planetary model best explains the observed data, we conducted a further grid search to check if there are any other local minima with different q values. In Figure 20, we plot $\Delta\chi^2$ for each model with a range of mass ratios q. Here, we searched for the best model using each q value leaving the other parameters to vary freely. The ranges of q, s, and α in this search are the same as those used in the first grid search. We found

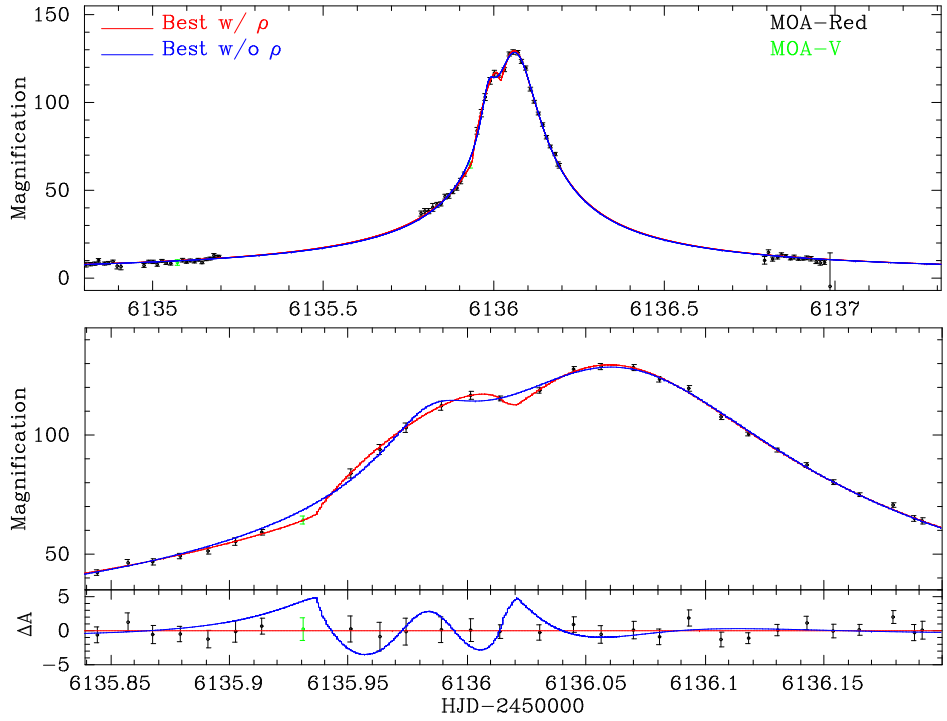

Figure 18: Best-fit model fitted with the finite source effect (red line) and the best model fitted without the finite source effect (blue line). The χ^2 of the blue line is $\Delta\chi^2 \sim 17.1$ larger than the red one.

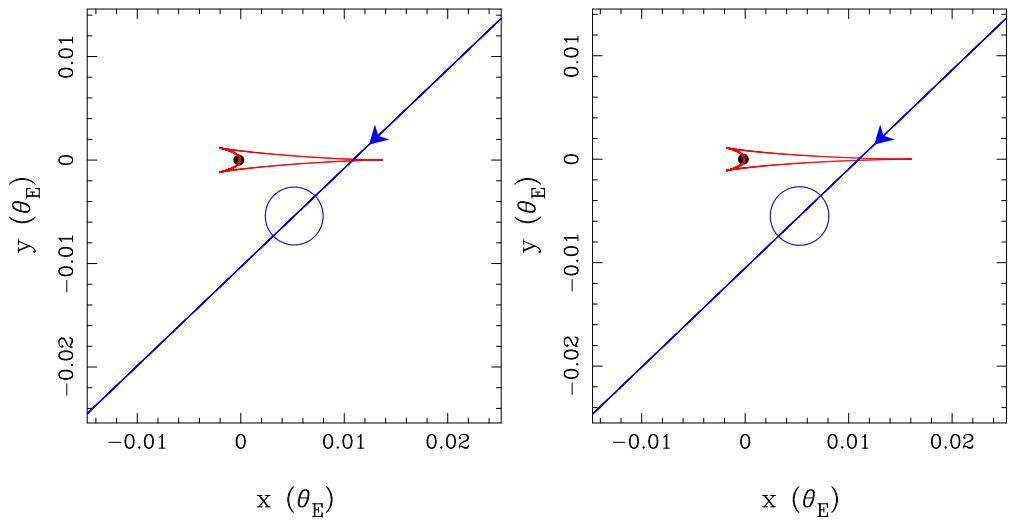

Figure 19: Caustic geometries for the best-fit close (left) and wide (right) models indicated by the red curves. The blue line for each of the figures shows the source trajectory with respect to the lens system. The blue circle for each of the figures indicates the source star size.

some local minima corresponding to distinctly different lens system geometries. Three of these minima can be seen in Figure 20 while the others have larger χ^2. Models in the range of $q \lesssim 4 \times 10^{-3}$, $4 \times 10^{-3} \lesssim q \lesssim 1 \times 10^{-2}$, and $q \gtrsim 1 \times 10^{-2}$ have the same sort of geometry as the best model with $(q, s, \alpha) = (2.1 \times 10^{-4}, 1.1, 2.4)$, another planetary solution with $(q, s, \alpha) = (5.2 \times 10^{-3}, 1.3, 5.0)$ and the stellar binary solution with $(q, s, \alpha) = (6.6 \times 10^{-2}, 0.2, 1.3)$, respectively. We found that the local minimum with $q \sim 6.63 \times 10^{-2}$ in Figure 20 is the only local minimum with a stellar mass ratio. This model corresponds to the second best model found from the first grid analysis above whose $\Delta\chi^2$ with respect to the best model is ~ 31 (i.e., larger than 5σ). Therefore, we conclude that the planetary solution is the global best solution for this event.

Because we were unable to detect the microlensing parallax in this event, we cannot determine the physical parameters of the lens system uniquely. Only the measurement of the finite source effect in this event partially breaks the degeneracy between microlensing parameters, which can be used to estimate the probability distribution of the physical parameters via the Bayesian analysis in Section A.5.

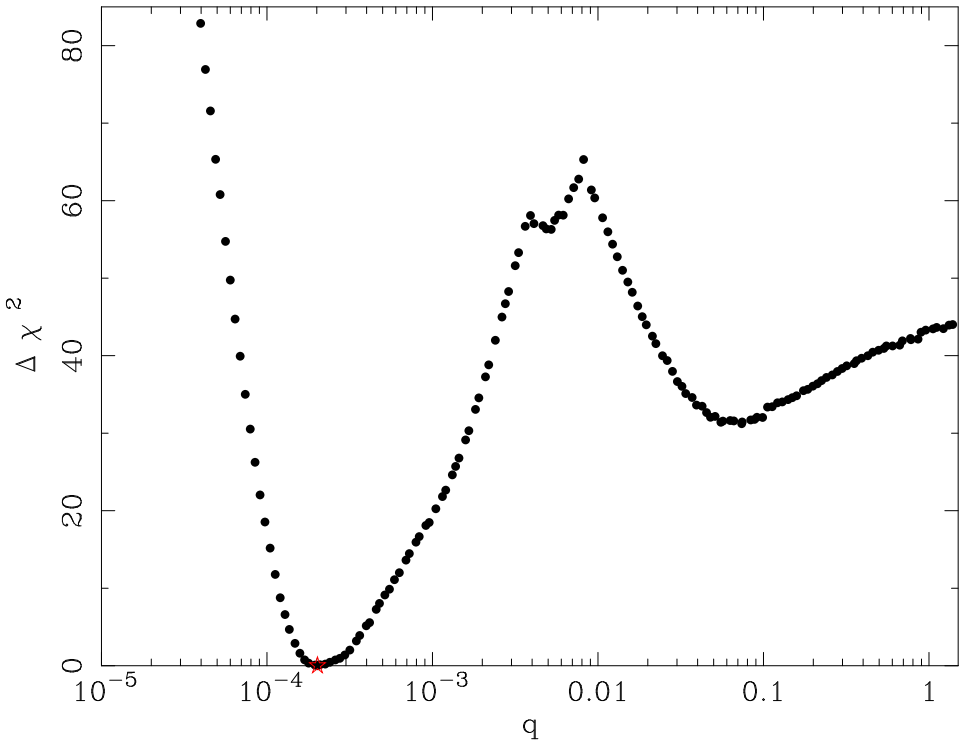

Figure 20: $\Delta\chi^2$ from the best-fit model as a function of q. The red star indicates the $\Delta\chi^2$ and q values corresponding to the best-fitting model. There is a local minimum at $q \sim 6.63 \times 10^{-2}$, and the $\Delta\chi^2$ between the best and local minimum is about 31.

A.4 CMD and Source Radius

In this section, we estimate the angular Einstein radius $\theta_{\rm E} = \theta_*/\rho$ from the best-fit ρ and the angular source radius θ_*, which can be calculated from the source color and magnitude. We get the source color and magnitude from MOA-Red band and MOA-V-band data. Figure 21 shows the OGLE (the Optical Gravitational Lensing Experiment; Udalski, 2003) $(V-I, I)$ color–magnitude diagram (CMD) of stars within $2'$ around MOA-2012-BLG-505 (Szymański et al., 2011). It also shows the deep CMD of Baade's window as observed by HST (Holtzman et al., 1998) and which is adjusted for the distance, reddening and extinction to the MOA-2012-BLG-505 field by using Red Clump Giants (RCG) as standard candles (Bennett et al., 2008). We convert the best-fit MOA-Red and MOA-V source magnitude to the standard Cousins I and Johnson V magnitude by cross-referencing stars in the MOA field with stars in the OGLE-III photometry map (Szymański et al., 2011) within $2'$ of the event. We find the source color and magnitude to be $(V-I, I)_{\rm S,OGLE} = (2.00, 21.29) \pm (0.06, 0.13)$. We only have a couple of MOA-V data points, one highly magnified point and one with low magnification, during this event. So we doubled the nominal error of the source color conservatively. We find, therefore, the source color and magnitude to be $(V-I, I)_{\rm S,OGLE} = (2.00, 21.29) \pm (0.12, 0.13)$. The centroid of RCG color and magnitude in CMD are $(V-I, I)_{\rm RCG} = (2.49, 16.32) \pm (0.01, 0.03)$ as shown in Figure 21. Comparing these values to the expected extinction-free RCG color and magnitude at this field of $(V-I, I)_{\rm RCG,0} = (1.06, 14.55) \pm (0.07, 0.04)$ (Bensby et al., 2013; Nataf et al., 2013), we get the reddening and extinction to the source of $(E(V-I), A_I)_{\rm RCG} = (1.43, 1.77) \pm (0.07, 0.05)$. Therefore, we estimated the extinction-free source color and magnitude as being

$$(V-I, I)_{\rm S,0} = (0.57, 19.52) \pm (0.14, 0.14). \tag{38}$$

By using the empirical formula, $\log(\theta_*) = 0.50141358 + 0.41968496(V-I) - 0.2I$ (Boyajian et al., 2014; Fukui et al., 2015), we estimated the angular source radius,

$$\theta_* = 0.34 \pm 0.05 \ \mu{\rm as}. \tag{39}$$

From this θ_* and other fitting parameters, we calculated the angular Einstein radius $\theta_{\rm E}$ and the lens–source relative proper motion $\mu_{\rm rel} = \theta_{\rm E}/t_{\rm E}$, as follows.

$$\theta_{\rm E} = 0.12 \pm 0.02 \ {\rm mas} \tag{40}$$

$$\mu_{\rm rel} = 4.40 \pm 0.72 \ {\rm mas \ yr^{-1}}. \tag{41}$$

This $\theta_{\rm E}$ is relatively small, which indicates that the lens is likely low-mass and/or far from the observer. This $\mu_{\rm rel}$ is relatively high, which prefers that the lens is in the Galactic bulge rather than the disk.

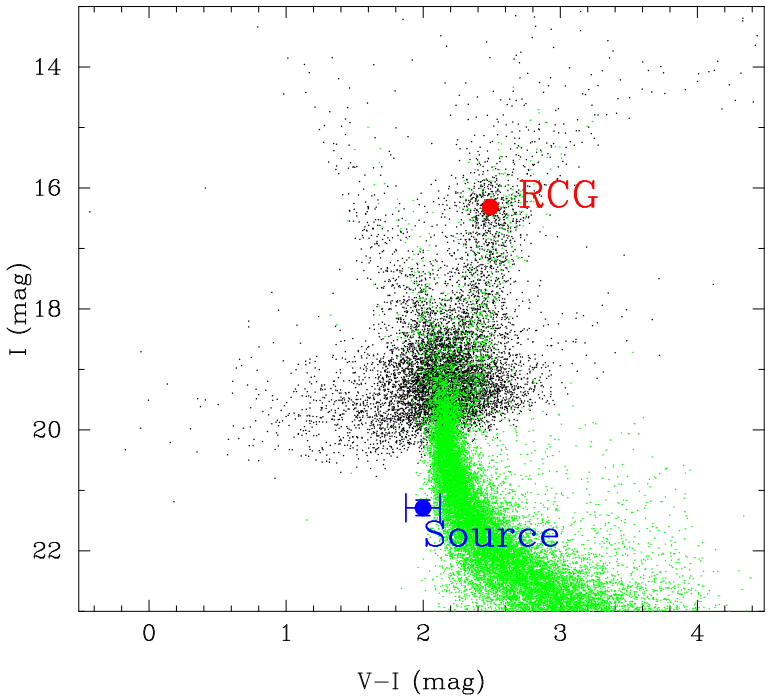

Figure 21: Color–magnitude diagram (CMD) of OGLE-III stars within 2′ of MOA-2012-BLG-505 (black dots). The green dots show the HST CMD (Holtzman et al., 1998). The red point indicates the centroid of the red clump giant, and the blue point indicates the source color and magnitude.

The source color obtained from MOA-Red and MOA-V data lies on the blue edge of the typical main-sequence stars expected from the HST CMD. We checked the effect of possible systematics in the color measurement on the final estimated lens physical parameters as follows. Assuming the source star is a main-sequence star in the Bulge, which is very likely, we adopt the mean color of the main-sequence stars in the HST CMD with the magnitudes ranging around the observed source magnitude $I_S = 21.29 \pm 0.13$ (Bennett et al., 2008). We get a source color and magnitude of $(V-I, I)_{\rm S,OGLE} = (2.32, 21.29) \pm (0.12, 0.13)$ and $(V-I, I)_{\rm S,0} = (0.89, 19.52) \pm (0.14, 0.14)$, with and without extinction and reddening, respectively.

The lens physical parameters estimated by using this source color are consistent with the final results by using the source color obtained from the light curves (see Section A.5) to within 1σ errors. Therefore, systematics in our measurement of the source color do not make any difference to our final results. We use the source color measured from the light curves in the following discussions.

A.5 Lens Physical Parameters by Bayesian Analysis

We cannot directly determine the lens physical parameters because we could not measure the microlensing parallax effect. Thus we estimated the probability distribution of lens physical properties by using a Bayesian analysis (Beaulieu et al., 2006; Gould et al., 2006; Bennett et al., 2008) assuming the Galactic model of Han & Gould (1995) as a prior probability. We note that the probability of stars hosting a planet with the measured q and s values is independent of the lens's mass and distance from the Earth. We used the measured $\theta_{\rm E}$ and $t_{\rm E}$ to constrain the probability distributions of lens parameters. Although this event has the $s \leftrightarrow 1/s$ degeneracy, all lens physical parameters of these degenerate solutions are consistent within the 68.3% confidence interval. Therefore, we combined the result of the wide and close model weighted by $e^{-\Delta\chi^2/2}$ ($\Delta\chi^2 = \chi^2_{close} - \chi^2_{wide} = 0.019$).

Planetary system parameters confidence intervals are sometimes set at the fixed contour levels, but this is confusing for distributions with multiple peaks. So, we prefer percentiles, so that the 68% and 95% confidence intervals represent the central 68% and 95% of the probability distribution. The posterior distributions and parameters are shown in Figure 22, Figure 23, and Table 5, respectively. According to this analysis, the host is a brown dwarf or late-M-dwarf with a mass of $0.10^{+0.16}_{-0.05} M_\odot$ at $7.21^{+1.14}_{-1.11}$kpc away from the Earth, i.e., likely in the Galactic bulge. In the calculation of the posterior probability, we treated the stars in the Bulge and the stars in the disk separately following each number density distributions given by Han & Gould (1995). The posterior probability that the lens system is in the bulge is 80.5%, and the

probability that the lens primary is a brown dwarf in the disk is 19.5%. The planet mass is a super-Earth with a mass of $6.7^{+10.7}_{-3.6} M_\oplus$, and the projected separation from the host is $r_\perp = 0.91^{+0.26}_{-0.23}$au. Assuming a planetary orbit with random inclination and phase (Gould & Loeb, 1992), the physical three-dimensional separation is $a = 1.13^{+0.68}_{-0.34}$au.

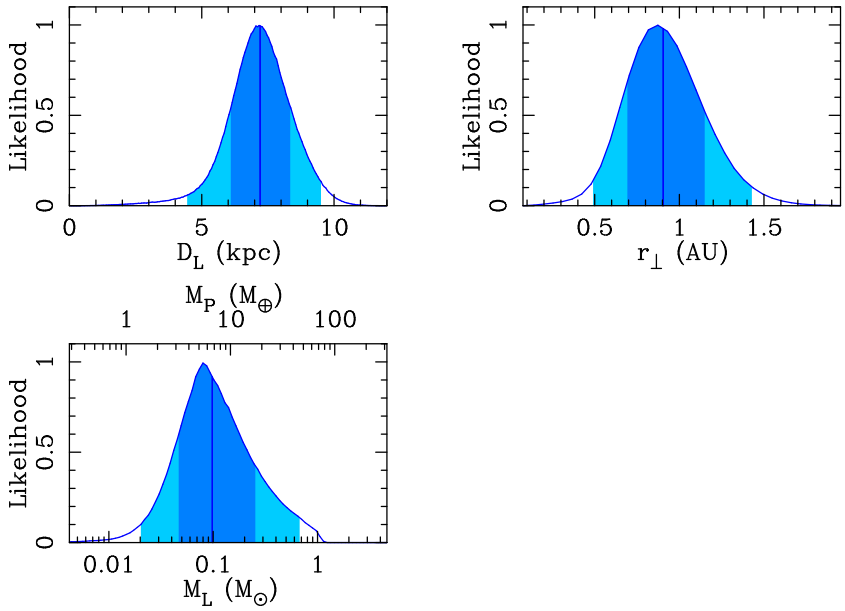

Figure 22: Relative probability distributions of lens system properties from our Bayesian analysis. The dark and light blue regions indicate the 68% and 95% confidence intervals respectively. The blue vertical lines indicate the median values of each of these distributions.

A.6 Discussion and Conclusion

We found that MOA-2012-BLG-505Lb is a super-Earth-mass planet, ranging from terrestrial mass to Neptune mass, orbiting around a brown dwarf or late-M dwarf probably in the Galactic bulge. Figure 24 shows the distribution of known exoplanets in planet mass as a function of the host mass. This event is shown by a purple circle and the position is in the bottom left (corresponding to both a low-mass host and planet). The red circles indicate the planets found by microlensing, where filled and open circles indicate that their masses are measured and estimated by a Bayesian

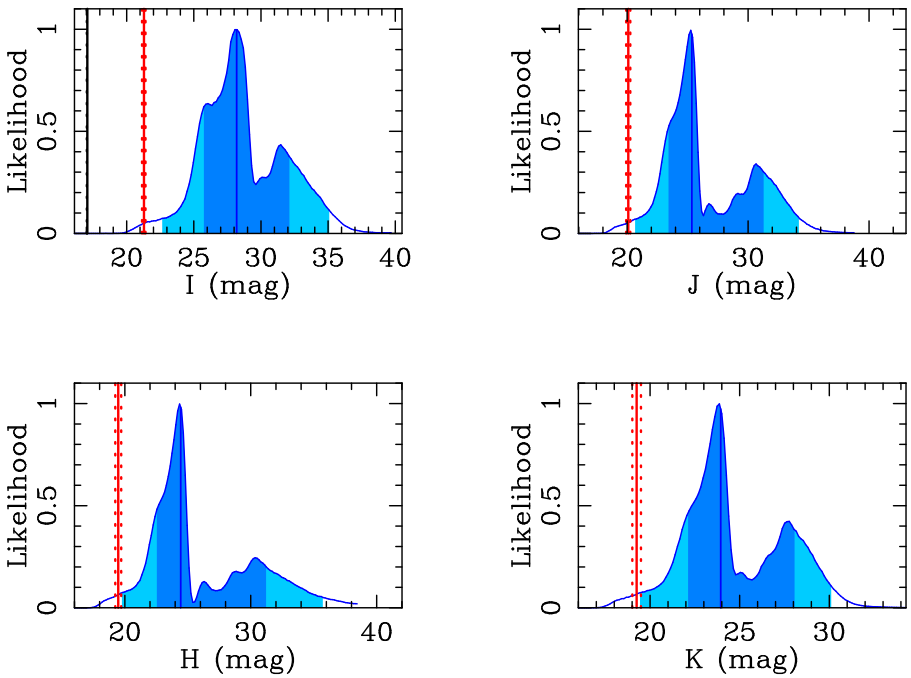

Figure 23: Relative probability distributions for the I-, J-, H-, and K-band lens star magnitudes from our Bayesian analysis with extinction. The dark and light blue regions indicate the 68% and 95% confidence intervals respectively. The vertical blue lines indicate the median values of each of these distributions. The vertical red lines indicate the source star magnitudes for each bands. Red dotted lines are their 1σ errors. The source magnitudes are estimated from Kenyon & Hartmann (1995) and Baraffe et al. (2003). Their extinctions are estimated from Cardelli et al. (1989).

analysis, respectively. Red ones indicate planetary mass ratios of $q \leq 0.1$ and green ones, on the other hand, indicate larger mass ratios of $q > 0.1$, i.e., low-mass binaries. Although the detection efficiencies of the planetary events with large q are higher than that with small q (Suzuki et al., 2016), all of planetary systems have small $q \sim 0.001 - 0.0001$ except one planetary system with large $q \sim 0.01$ (Han et al., 2016) orbiting around low-mass stars of $< 0.15 M_{\odot}$. This result indicates that the low-mass stars tend to host relatively low-mass planetary companions.

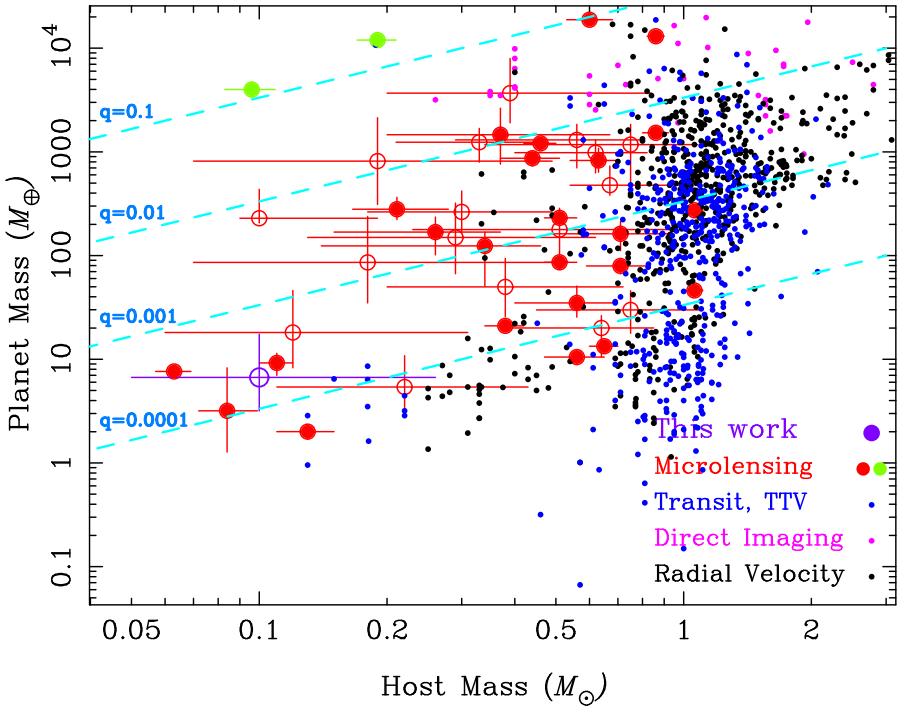

Figure 24: Distribution of exoplanets. The horizontal axis corresponds to the host mass and the vertical axis corresponds to the planet mass. The purple point indicates MOA-2012-BLG-505. The red, green, blue, magenta, and black points indicate the planets found by Microlensing (planetary mass companion), Microlensing (binary mass companion), Transit & TTV, Direct Imaging, and Radial Velocity, respectively. In microlensing planets, filled circles indicate that their masses are measured and open circles indicate that their masses are estimated by a Bayesian analysis. The values of microlensing planets are from the literature, while those of the others are from http://exoplanet.eu.

This event is roughly tied for the second shortest $t_{\rm E} \approx 10\,$days with a

planetary companion with OGLE-2016-BLG-1195 (Bond et al., 2017; Shvartzvald et al., 2017). The shortest duration event with a planetary mass ratio companion was MOA-2011-BLG-262 (Bennett et al., 2014). Only a few microlensing planets with $t_{\rm E} \lesssim 10$ days have been found. This is largely because the detection efficiency of planets in short events is low (Suzuki et al., 2016). We need to find and analyze more events like MOA-2012-BLG-505, to obtain unbiased statistics of planets around low-mass hosts.

The microlensing method has the capability to determine the dependence of the distribution of exoplanets on the distance from the center of our Galaxy. The comparison of published planets by Penny et al. (2016) is not conclusive because of biases in the planetary sample and the lack of a proper detection efficiency calculation for this sample. Large statistical samples (Suzuki et al., 2016) could be used for such a comparison if they are supplemented by lens mass measurements via a microlensing parallax (Gaudi et al., 2008; Bennett et al., 2014; Muraki et al., 2011) or host-star brightness measurements (Bennett et al., 2006, 2015; Batista et al., 2015). However, both of these methods are more effective for planetary systems in the disk. Space-based microlensing parallax measurements have somewhat of an advantage in this regard, though the Spitzer program is limited in its sensitivity to short duration events due to the necessity of identifying targets from ground-based data (Zhu et al., 2017). The Kepler $K2$ microlensing program is limited by its short duration (Henderson et al., 2016). Prior to this paper, there have been five planets located with a 1σ distance lower limit of $D_{\rm L} > 6.0$ kpc, i.e., they are likely to be in the Bulge. MOA-2011-BLG-028Lb (Skowron et al., 2016) was determined to be in the bulge due to an upper limit on the microlensing parallax, and MOA-2011-BLG-293Lb (Batista et al., 2014) was determined to be in the bulge by detection of the lens star. MOA-2008-BLG-310Lb (Janczak et al., 2010), OGLE-2015-BLG-0051Lb (Han et al., 2016), and MOA-2011-BLG-322Lb (Shvartzvald et al., 2014) were estimated to be in the bulge based on a Bayesian analysis that assumed that bulge and disk stars are equally likely to host planets, so these bulge planet identifications are less definitive than the first two. MOA-2011-BLG-028Lb, MOA-2008-BLG-310Lb and OGLE-2015-BLG-0051Lb are expected to be a Neptune-mass planet, sub-Saturn mass planet and a sub-Jupiter mass planet in the Galactic bulge, respectively. MOA-2011-BLG-293Lb and MOA-2011-BLG-322Lb are super-Jupiter mass planets in the Galactic bulge. The MOA-2011-BLG-262L host has an unusually high $\mu_{\rm rel}$, which combined with the small $t_{\rm E}$ implies a low-mass stellar host in the bulge or an apparently unbound planet hosting an Earth-mass moon. The Bayesian analysis for the OGLE-2016-BLG-1195 planetary system indicates a bulge lens (Bond et al., 2017), but the analysis of Spitzer data (Shvartzvald et al., 2017) seems to indicate a microlensing parallax signal due to a star in the disk that is not rotating with the disk.

The priori probability of microlensing parallax direction given its magnitude and the measured $\mu_{\rm rel}$ value is ~ 0.003. This suggests that the parallax measurement may have been compromised by a companion to the source or lens, so the nature of this event is as yet undetermined. Due to these ambiguities with MOA-2011-BLG-262Lb and OGLE-2016-BLG-1195Lb, MOA-2012-BLG-505Lb is the sixth planet that is likely to be in the Bulge. However, the possibility that it is a planet orbiting a brown dwarf in the disk cannot be ruled out. Nevertheless, this discovery contributes to the statistics of planet distribution in our Galaxy.

We used the Bayesian analysis to estimate the probability distribution of the lens physical parameters because we could not measure the microlensing parallax. It is difficult to observe the microlensing parallax in the Bulge lens events because they are relatively short and their projected Einstein radius on the observer plane, $\tilde{r}_{\rm E}$ is large relative to 1 au. $\tilde{r}_{\rm E}$ for the Bulge lens event is $3 \sim 10$au typically. It is difficult to detect the microlensing parallax for such events from the space telescope located at L2, however we may be able to detect these from the telescope located on $\sim$ au away from the Earth like Spitzer (Street et al., 2016) and/or Kepler (Henderson et al., 2016). If these instruments observe many events similar to MOA-2012-BLG-505, they will be able to determine the planet distribution in the Galaxy down to low-mass hosts. NASA's $WFIRST$ satellite will increase this sample size significantly and reveal the Galactic distribution of exoplanets (Spergel et al., 2015).

We may identify the lens by future high-resolution imaging with space telescope or ground-based AO observations if it is a relatively massive star, or we may set a tight upper limit when it is a really low-mass star. Figure 23 shows the distributions of I-, J-, H-, and K-band magnitudes for the lens star with extinction. The lens magnitudes are estimated from Kenyon & Hartmann (1995) and Baraffe et al. (2003). We selected the isochrone model for a 5 Gyr brown dwarf from Baraffe et al. (2003). The extinctions are estimated by using Cardelli et al. (1989). The distributions look bimodal because the luminosity changes sharply around $0.07 M_\odot$, i.e., at the boundary between brown-dwarf and main-sequence stars, in the mass–luminosity relation. We cannot detect the lens star if it is a brown dwarf. However, if the lens star is a hydrogen burning star, we will probably be able to detect it with $JWST$ (Gardner et al., 2006) when it is separated from the source star after 10 years.

Table 4: The Best-fit Parameters and 1σ Errors for Close and Wide Models

Parameter Error (1σ)	Units	Close ($s < 1$)	Wide ($s > 1$)
t_0	HJD–2450000	6136.0557	6136.0558
		0.0005	0.0005
t_E	days	10.0133	9.8335
		1.0035	1.0506
u_0	10^{-3}	7.4775	7.6002
		0.8810	0.8568
q	10^{-4}	2.0520	2.0521
		0.5647	0.5528
s		0.8928	1.1266
		0.0477	0.0653
α	radians	2.3794	2.3782
		0.0175	0.0160
ρ	10^{-3}	2.7971	2.8322
		0.3714	0.3703
θ_*	μas	0.342	0.342
		0.052	0.052
$\theta_{\rm E}$	mas	0.122	0.121
		0.025	0.024
$\mu_{\rm rel}$	mas yr^{-1}	4.3890	4.3971
		0.7198	0.7196
dof	$\cdots$	16004	16004
χ^2	$\cdots$	16010.859	16010.840

Table 5: The physical parameters and 1σ errors of MOA-2012-BLG-505

Parameter	Units	Value	Error(1σ)
$D_{\rm L}$	kpc	7.21	$^{+1.14}_{-1.11}$
$M_{\rm L}$	$M_\odot$	0.10	$^{+0.16}_{-0.05}$
$m_{\rm p}$	$M_\oplus$	6.70	$^{+10.61}_{-3.51}$
$r_\perp$	au	0.90	$^{+0.25}_{-0.21}$
a	au	1.12	$^{+0.67}_{-0.32}$
μ	$\mathrm{mas\,yr^{-1}}$	4.72	$^{+1.01}_{-0.91}$
J	mag	25.34	$^{+5.94}_{-1.92}$
H	mag	24.43	$^{+6.79}_{-1.89}$
K	mag	23.93	$^{+4.13}_{-1.82}$

Appendix B Additional Discussion

B.1 Which do microlensing planets favor, the core accretion model or the disk instability model?

The result of the *Kepler* transit survey suggests that terrestrial-mass planets are far more numerous than Jovian-mass planets for orbital periods up to 85 days (Fressin et al., 2013). This statistical study may support the core accretion model (Safronov, 1972; Hayashi et al., 1985; Lissauer, 1993); however, this is limited to the planets orbiting inside of the snow-line around the solar-type stars (Figure 25). The planet distribution and planet formation around M-dwarfs are not yet understood well, even though the M-dwarfs are the most abundant star in the Galaxy. Besides, it is difficult to detect the planet around an M-dwarf with radial velocity method because the brightness of M-dwarf itself is faint in optical wavelength and most of M-dwarfs have strong stellar chromospheric activities. Nevertheless, the planets around M-dwarfs have been recently detected by the radial velocity observations, e.g. Calar Alto high-Resolution search for M dwarfs with Exoearths with Near-infrared and optical Echelle Spectrographs (CARMENES; Quirrenbach et al. 2014) and the High Accuracy Radial velocity Planet Searcher for the Northern hemisphere (HARPS-N; Cosentino et al. 2012). GJ 3512 b is one of the giant planets hosted by M-dwarfs, and especially the first detection of the sub-Jupiter mass planet with a minimum mass of $M_{\rm p}{\rm sin}i = 0.46 \pm 0.02\,M_{\rm Jup}$ around a very-low-mass M-dwarf with a mass of $M_{\rm Host} = 0.12 \pm 0.01\,M_{\odot}$ orbiting at 0.34 ± 0.01 au away from its host star, i.e., beyond the snow-line by the radial velocity method (Morales et al., 2019). Figure 26 shows the distribution of exoplanets around M-dwarfs. According to this figure, the exoplanets beyond the snow-line of M-dwarfs are discovered by the microlensing method, the radial velocity method, and the direct imaging, and this indicates that a decent amount of giant exoplanets could exist outside of the snow-line of M-dwarfs (Bonfils et al., 2013; Clanton, & Gaudi, 2014). The formation of a super-Earth mass planet around a late-M-dwarf, such as MOA-2012-BLG-505Lb (Nagakane et al., 2017), could be described by the standard core accretion model. On the other hand, OGLE-2015-BLG-1649Lb, a massive planet around an M-dwarf (Nagakane et al., 2019) may support the disk instability model (Boss, 2006). These studies suggest that both core accretion and disk instability could occur outside of the snow-line of M-dwarfs. Meanwhile, Santos et al. (2017) and Schlaufman (2018) suggested that there is a population boundary at $\sim 4\,M_{\rm Jup}$ and $\sim 10\,M_{\rm Jup}$ around the solar-type stars, respectively. This may indicate that the planet formation process shifts from the standard core accretion model to the disk instability model around the boundary. However, such statistical studies have not

conducted yet for the planets outside snow-line around M-dwarfs because there are still not many samples especially outside of the snow-line. To put the constraint on the planet formation theory, we need to reveal the planet frequency both inside and outside of the snow-line around M-dwarfs. In the future, it will be possible to increase the number of exoplanets orbiting inside of the snow-line by Transiting Exoplanet Survey Satellite (TESS; Ricker et al. 2015), Subaru/IRD (Tamura et al., 2012), and the PLAnetary Transits and Oscillations of stars (PLATO; Rauer et al. 2014); whereas the number of exoplanets orbiting outside of the snow-line will be increased mainly by the microlensing observation.

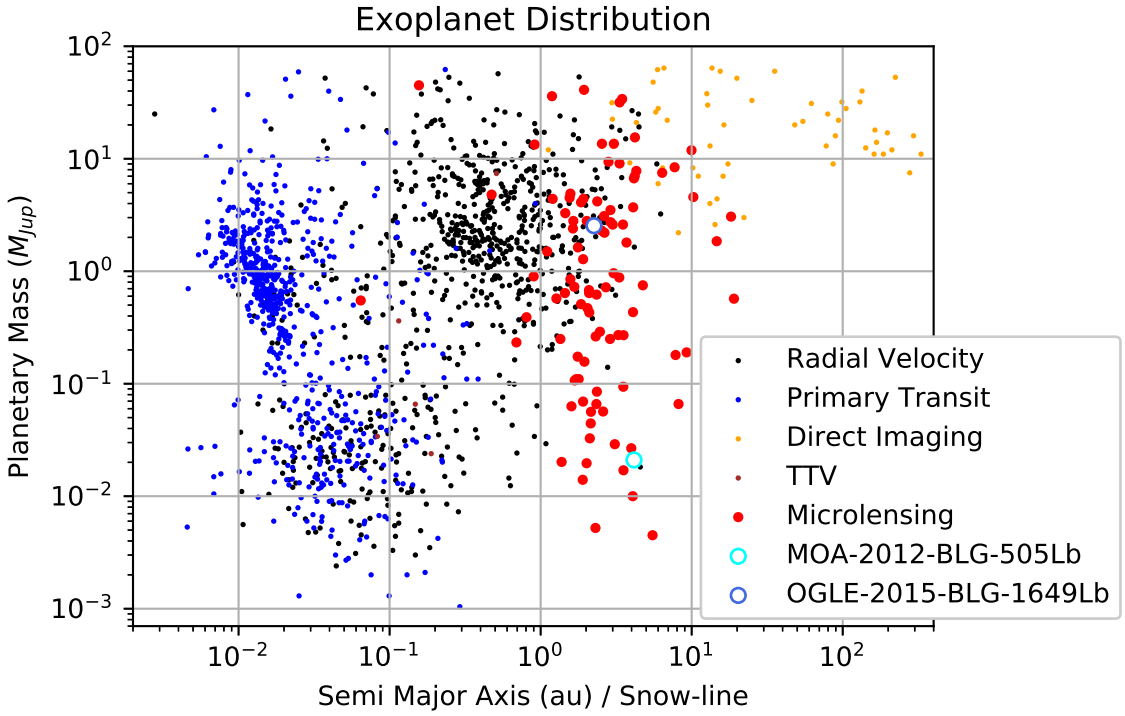

Figure 25: Distribution of exoplanets. The vertical axis and horizontal axis correspond to the planet mass and the semi-major axis normalized by the snow-line which is assumed to depend on the host star mass as $\sim 2.7\,\mathrm{au}\,(M/M_\odot)$ (Kennedy, & Kenyon, 2008), respectively. The light-blue and dark-blue circles indicate MOA-2012-BLG-505Lb and OGLE-2015-BLG-1649Lb, respectively. The values are from http://exoplanet.eu.

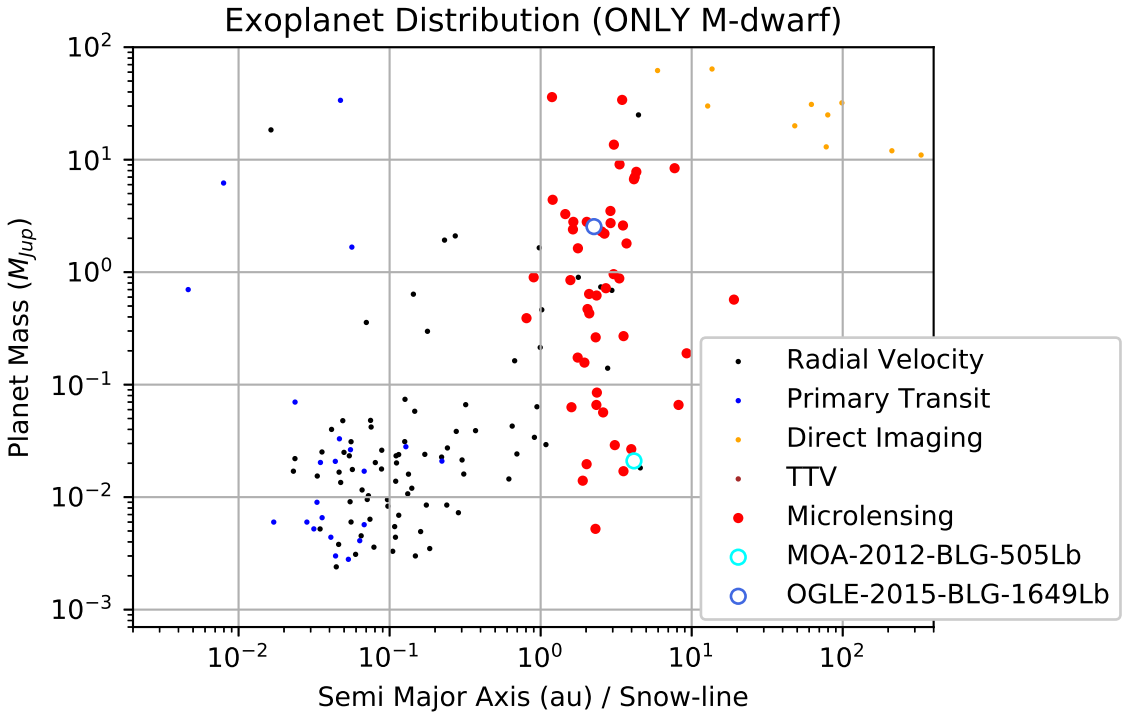

Figure 26: The same distribution as Figure 25, but only M-dwarf host stars ($0.08\,M_{\odot} < M_{\rm Host} < 0.5\,M_{\odot}$) are plotted. The values are from http://exoplanet.eu.

B.2 Does the peak in the planet mass function depend on the host star mass?

MOA-2012-BLG-505Lb is one of the samples used in Suzuki et al. (2016). This event has a mass ratio of 2.1×10^{-4} which is near the break of mass ratio function $q_{break} \sim 1.7 \times 10^{-4}$ estimated in that study. Suzuki et al. (2016) estimated that the q_{break} corresponds to $\sim 20\,M_{\oplus}$ for the median host star mass of $\sim 0.6\,M_{\odot}$. However, since the host star mass of MOA-2012-BLG-505L is much lower than that, the planet mass should be lower than Neptune mass. Thus, this event suggests that the true mass of the q_{break} could range over one dex if the q_{break} is a universal value for the main sequence star. Jung et al. (2019) also estimated the mass-ratio break of $q_{break} \sim 5.5 \times 10^{-5}$ from the microlensing sample. this study also did not classify the host star mass in their sample. Therefore, it is necessary to examine the mass ratio function for each star mass in order to understand the planet distribution in more detail. Pascucci et al. (2018) classified the *Kepler* samples into the spectral type of host stars and estimated the break in the mass-ratio function for each spectral type samples. They found the break in the mass-ratio function is almost the same for the G, K, M-type stars.

In this thesis, the similar work with Pascucci et al. (2018) for the microlensing planets is conducted. Here we use the published microlensing planets from http://exoplanet.eu for this analysis. However, the published planets are classified into two according to their host star masses because the number of samples is not large enough. Figure 27 shows the histogram of the microlensing planets as a function of mass ratio classified by $M_{\rm Host} < 0.5 M_{\odot}$ and $M_{\rm Host} > 0.5 M_{\odot}$. The former is indicated with cyan and the latter is indicated with magenta. In this histogram, the number of planets per one detection is corrected by an approximate relative detection efficiency of $(q/q_{\rm Jup})^{\alpha}$, where q is the planet–host mass ratio and $q_{\rm Jup} \equiv M_{\rm Jup}/0.35 M_{\odot}$. Here, the assumption of $\alpha = 0.6$ is applied for all planets as a mean value for the central-caustic and planetary-caustic crossing or approaching events (Sumi et al., 2010; Fukui et al., 2015). According to this figure, it seems that the peaks appear to occur at $q \sim 10^{-4}$ for both classifications. Note that assuming the uncertainty of the mass ratio for the peak is factor 2, this value is roughly consistent with those from Suzuki et al. (2016) and Jung et al. (2019). The fact that the peaks in the mass ratio function for both classifications have almost identical value would suggest that the mass at the peak in the planet mass function depends on the host star mass. Therefore, this analysis found for the first time that the mass-ratio could be a universal parameter to describe the planet distribution from the inside (as indicated in Pascucci et al. 2018) to outside of the snow-line. Note that this histogram includes a large number of microlensing planets whose mass was estimated by using a Bayesian analysis. To evaluate the break more precisely, a large

amount of microlensing planets with mass measurements is required. Therefore, it is important to increase the number of events whose masses are constrained by the lens flux, such as OGLE-2015-BLG-1649 (Nagakane et al., 2019). Moreover, the future microlensing survey by the PRime-focus Infrared Microlensing Experiment (PRIME) telescope that is under construction and the *WFIRST* space telescope will achieve the requirement.

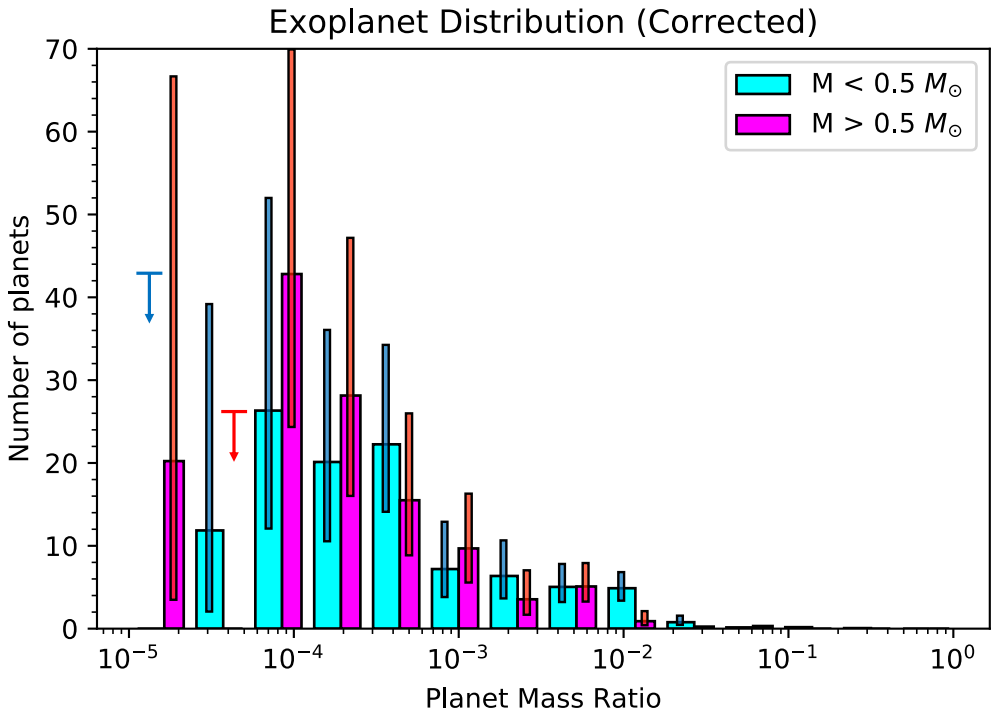

Figure 27: Histogram of the microlensing planets as a function of mass ratio. The values are from http://exoplanet.eu.

References

Alcock, C., Akerlof, C. W., Allsman, R. A., et al. 1993, Nature, 365, 621

Alcock, C., Allsman, R. A., Axelrod, T. S., et al. 1993, Sky Surveys. Protostars to Protogalaxies, 291

Aubourg, E., Bareyre, P., Brehin, S., et al. 1993, The Messenger, 72, 20

Baraffe, I., Chabrier, G., Barman, T. S., Allard, F., & Hauschildt, P. H. 2003, Astronomy & Astrophysics, 402, 701

Batalha, N. M., Rowe, J. F., Bryson, S. T., et al. 2013, The Astrophysical Journal Supplement Series, 204, 24

Batista, V., Beaulieu, J.-P., Gould, A., et al. 2014, The Astrophysical Journal, 780, 54

Batista, V., Beaulieu, J.-P., Bennett, D.P., et al. 2015, The Astrophysical Journal, 808, 170

Beaulieu, J.-P., Bennett, D. P., Fouqué, P., et al. 2006, Nature, 439, 437

Bennett, D. P. 2010, The Astrophysical Journal, 716, 1408

Bennett, D. P., Anderson, J., Bond, I. A., Udalski, A., & Gould, A. 2006, The Astrophysical Journal Letters, 647, L171

Bennett, D. P., Anderson, J., & Gaudi, B. S. 2007, The Astrophysical Journal, 660, 781

Bennett, D. P., Batista, V., Bond, I. A., et al. 2014, The Astrophysical Journal, 785, 155

Bennett, D. P., Bhattacharya, A., Anderson, J., et al. 2015, The Astrophysical Journal, 808, 169

Bennett, D. P., Bond, I. A., Udalski, A., et al. 2008, The Astrophysical Journal, 684, 663-683

Bennett, D. P., & Rhie, S. H. 1996, The Astrophysical Journal, 472, 660

Bennett, D. P., & Rhie, S. H. 2002, The Astrophysical Journal, 574, 985

Bensby, T., Yee, J. C., Feltzing, S., et al. 2013, Astronomy & Astrophysics, 549, A147

Bhattacharya, A., Beaulieu, J.-P., Bennett, D. P., et al. 2018, The Astronomical Journal, 156, 289

Bhattacharya, A., Bennett, D. P., Anderson, J., et al. 2017, The Astronomical Journal, 154, 59

Bond, I. A., Abe, F., Dodd, R. J., et al. 2001, Monthly Notices of the Royal Astronomical Society, 327, 868

Bond, I. A., Bennett, D. P., Sumi, T., et al. 2017, arXiv:1703.08639

Bond, I. A., Udalski, A., Jaroszyński, M., et al. 2004, The Astrophysical Journal Letters, 606, L155

Bonfils, X., Delfosse, X., Udry, S., et al. 2013, Astronomy & Astrophysics, 549, A109

Borucki, W. J., Koch, D., Basri, G., et al. 2010, Science, 327, 977

Borucki, W. J., Koch, D. G., Basri, G., et al. 2011, The Astrophysical Journal, 736, 19

Boss, A. P. 1997, Science, 276, 1836

Boss, A. P. 2006, The Astrophysical Journal Letters, 644, L79

Boyajian, T. S., van Belle, G., & von Braun, K. 2014, The Astronomical Journal, 147, 47

Bramich, D. M. 2008, Monthly Notices of the Royal Astronomical Society, 386, L77

Bramich, D. M., Horne, K., Albrow, M. D., et al. 2013, Monthly Notices of the Royal Astronomical Society, 428, 2275

Brown, T. M., Baliber, N., Bianco, F. B., et al. 2013, Publications of the Astronomical Society of the Pacific, 125, 1031

Butler, R. P., Wright, J. T., Marcy, G. W., et al. 2006, The Astrophysical Journal, 646, 505

Cameron, A. G. W. 1978, Moon and Planets, 18, 5

Cardelli, J. A., Clayton, G. C., & Mathis, J. S. 1989, The Astrophysical Journal, 345, 245

Carpenter, J. M. 2001, The Astronomical Journal, 121, 2851

Charbonneau, D., Brown, T. M., Latham, D. W., & Mayor, M. 2000, The Astrophysical Journal Letters, 529, L45

Choi, J.-Y., Shin, I.-G., Park, S.-Y., et al. 2012, The Astrophysical Journal, 751, 41

Chwolson, O. 1924, Astronomische Nachrichten, 221, 329

Clanton, C., & Gaudi, B. S. 2014, The Astrophysical Journal, 791, 91

Claret, A. 2000, Astronomy & Astrophysics, 363, 1081

Claret, A., & Bloemen, S. 2011, Astronomy & Astrophysics, 529, A75

Cosentino, R., Lovis, C., Pepe, F., et al. 2012, Proceedings of SPIE, 84461V

Dominik, M., Jørgensen, U. G., Rattenbury, N. J., et al. 2010, Astronomische Nachrichten, 331, 671

Einstein, A. 1936, Science, 84, 506

Evans, D. F., Southworth, J., Maxted, P. F. L., et al. 2016, Astronomy & Astrophysics, 589, A58

Fressin, F., Torres, G., Charbonneau, D., et al. 2013, The Astrophysical Journal, 766, 81

Fukui, A., Gould, A., Sumi, T., et al. 2015, The Astrophysical Journal, 809, 74

Gardner, J. P., Mather, J. C., Clampin, M., et al. 2006, Space Science Reviews, 123, 485

Gaudi, B. S. 2012, Annual Review of Astronomy and Astrophysics, 50, 411

Gaudi, B. S., Bennett, D. P., Udalski, A., et al. 2008, Science, 319, 927

González Hernández, J. I., & Bonifacio, P. 2009, Astronomy & Astrophysics, 497, 497

Gould, A. 1992, The Astrophysical Journal, 392, 442

Gould, A., & Loeb, A. 1992, The Astrophysical Journal, 396, 104

Gould, A., Udalski, A., An, D., et al. 2006, The Astrophysical Journal Letters, 644, L37

Griest, K., & Safizadeh, N. 1998, The Astrophysical Journal, 500, 37

Han, C., & Gould, A. 1995, The Astrophysical Journal, 447, 53

Han, C., Udalski, A., Gould, A., et al. 2016, The Astronomical Journal, 152, 95

Hayano, Y., Takami, H., Oya, S., et al. 2010, Proceedings of SPIE, 7736, 77360N

Hayashi, C., Nakazawa, K., & Nakagawa, Y. 1985, Protostars and Planets II, 1100

Henderson, C. B., Poleski, R., Penny, M., et al. 2016, Publications of the Astronomical Society of the Pacific, 128, 124401

Henderson, C. B., & Shvartzvald, Y. 2016, The Astronomical Journal, 152, 96

Hirao, Y., Udalski, A., Sumi, T., et al. 2016, The Astrophysical Journal, 824, 139

Holtzman, J. A., Watson, A. M., Baum, W. A., et al. 1998, The Astronomical Journal, 115, 1946

Ida, S., & Lin, D. N. C. 2004, The Astrophysical Journal, 604, 388

Ida, S., & Lin, D. N. C. 2004, The Astrophysical Journal, 616, 567

Ida, S., & Lin, D. N. C. 2005, Progress of Theoretical Physics Supplement, 158, 68

Ida, S., & Lin, D. N. C. 2010, The Astrophysical Journal, 719, 810

Ida, S., Lin, D. N. C., & Nagasawa, M. 2013, The Astrophysical Journal, 775, 42

Janczak, J., Fukui, A., Dong, S., et al. 2010, The Astrophysical Journal, 711, 731

Jung, Y. K., Gould, A., Zang, W., et al. 2019, The Astronomical Journal, 157, 72

Kennedy, G. M., & Kenyon, S. J. 2008, The Astrophysical Journal, 673, 502

Kennedy, G. M., Kenyon, S. J., & Bromley, B. C. 2006, The Astrophysical Journal Letters, 650, L139

Kenyon, S. J., & Hartmann, L. 1995, The Astrophysical Journal Supplement Series, 101, 117

Kim, S.-L., Lee, C.-U., Park, B.-G., et al. 2016, Journal of Korean Astronomical Society, 49, 37

Kobayashi, N., Tokunaga, A. T., Terada, H., et al. 2000, Proceedings of SPIE, 4008, 1056

Koshimoto, N., Bennett, D. P., & Suzuki, D. 2019, arXiv e-prints, arXiv:1910.11448

Koshimoto, N., Shvartzvald, Y., Bennett, D. P., et al. 2017, The Astronomical Journal, 154, 3

Koshimoto, N., Udalski, A., Sumi, T., et al. 2014, The Astrophysical Journal, 788, 128

Laughlin, G., Bodenheimer, P., & Adams, F. C. 2004, The Astrophysical Journal Letters, 612, L73

Liebes, S. 1964, Physical Review, 133, 835

Lin, D. N. C., Bodenheimer, P., & Richardson, D. C. 1996, Nature, 380, 606

Lin, D. N. C., & Ida, S. 1997, The Astrophysical Journal, 477, 781

Lissauer, J. J. 1993, Annual Review of Astronomy and Astrophysics, 31, 129

Macintosh, B., Graham, J. R., Barman, T., et al. 2015, Science, 350, 64

Mao, S., & Paczyński, B. 1991, The Astrophysical Journal Letters, 374, L37

Mayor, M., & Queloz, D. 1995, Nature, 378, 355

Minniti, D., Lucas, P. W., Emerson, J. P., et al. 2010, New Astronomy, 15, 433

Morales, J. C., Mustill, A. J., Ribas, I., et al. 2019, Science, 365, 1441

Muraki, Y., Han, C., Bennett, D. P., et al. 2011, The Astrophysical Journal, 741, 22

Nagakane, M., Sumi, T., Koshimoto, N., et al. 2017, The Astronomical Journal, 154, 35

Nagakane, M., Lee, C.-H., Koshimoto, N., et al. 2019, The Astronomical Journal, 158, 212

Nataf, D. M., Gonzalez, O. A., Casagrande, L., et al. 2016, Monthly Notices of the Royal Astronomical Society, 456, 2692

Nataf, D. M., Gould, A., Fouqué, P., et al. 2013, The Astrophysical Journal, 769, 88

Paczynski, B. 1986, The Astrophysical Journal, 304, 1

Pascucci, I., Mulders, G. D., Gould, A., et al. 2018, The Astrophysical Journal Letters, 856, L28

Penny, M. T., Gaudi, B. S., Kerins, E., et al. 2019, The Astrophysical Journal Supplement Series, 241, 3

Penny, M. T., Henderson, C. B., & Clanton, C. 2016, The Astrophysical Journal, 830, 150

Pepe, F., Molaro, P., Cristiani, S., et al. 2014, Astronomische Nachrichten, 335, 8

Quirrenbach, A., Amado, P. J., Caballero, J. A., et al. 2014, Proceedings of SPIE, 91471F

Rasio, F. A., & Ford, E. B. 1996, Science, 274, 954

Rattenbury, N. J., Bond, I. A., Skuljan, J., & Yock, P. C. M. 2002, Monthly Notices of the Royal Astronomical Society, 335, 159

Rauer, H., Catala, C., Aerts, C., et al. 2014, Experimental Astronomy, 38, 249

Rhie, S. H., Bennett, D. P., Becker, A. C., et al. 2000, The Astrophysical Journal, 533, 378

Ricker, G. R., Winn, J. N., Vanderspek, R., et al. 2015, Journal of Astronomical Telescopes, Instruments, and Systems, 1, 014003

Safronov, V. S. 1972, Evolution of the protoplanetary cloud and formation of the earth and planets., by Safronov, V. S.. Translated from Russian. Jerusalem (Israel): Israel Program for Scientific Translations, Keter Publishing House, 212 p.,

Sako, T., Sekiguchi, T., Sasaki, M., et al. 2008, Experimental Astronomy, 22, 51

Santos, N. C., Adibekyan, V., Figueira, P., et al. 2017, Astronomy & Astrophysics, 603, A30

Schlaufman, K. C. 2018, The Astrophysical Journal, 853, 37

Shvartzvald, Y., & Maoz, D. 2012, Monthly Notices of the Royal Astronomical Society, 419, 3631

Shvartzvald, Y., Maoz, D., Kaspi, S., et al. 2014, Monthly Notices of the Royal Astronomical Society, 439, 604

Shvartzvald, Y., Yee, J. C., Calchi Novati, S., et al. 2017, The Astrophysical Journal Letters, 840, L3

Skottfelt, J., Bramich, D. M., Hundertmark, M., et al. 2015, Astronomy & Astrophysics, 574, A54

Skowron, J., Udalski, A., Poleski, R., et al. 2016, The Astrophysical Journal, 820, 4

Skrutskie, M. F., Cutri, R. M., Stiening, R., et al. 2006, The Astronomical Journal, 131, 1163

Spergel, D., Gehrels, N., Baltay, C., et al. 2015, arXiv:1503.03757

Street, R. A., Bachelet, E., Tsapras, Y., et al. 2019, The Astronomical Journal, 157, 215

Street, R. A., Udalski, A., Calchi Novati, S., et al. 2016, The Astrophysical Journal, 819, 93

Sumi, T., Abe, F., Bond, I. A., et al. 2003, The Astrophysical Journal, 591, 204

Sumi, T., Bennett, D. P., Bond, I. A., et al. 2010, The Astrophysical Journal, 710, 1641

Suzuki, D., Bennett, D. P., Ida, S., et al. 2018, The Astrophysical Journal Letters, 869, L34

Suzuki, D., Bennett, D. P., Sumi, T., et al. 2016, The Astrophysical Journal, 833, 145

Szymański, M. K., Udalski, A., Soszyński, I., et al. 2011, Acta Astronomica, 61, 83

Tamura, M., Suto, H., Nishikawa, J., et al. 2012, Proceedings of SPIE, 84461T

Tsapras, Y., Street, R., Horne, K., et al. 2009, Astronomische Nachrichten, 330, 4

Udalski, A. 2003, Acta Astronomica, 53, 291

Udalski, A., Szymanski, M., Kaluzny, J., et al. 1992, Acta Astronomica, 42, 253

Udalski, A., Szymanski, M., Kaluzny, J., et al. 1993, Acta Astronomica, 43, 289

Udalski, A., Szymański, M. K., & Szymański, G. 2015, Acta Astronomica, 65, 1

Verde, L., Peiris, H. V., Spergel, D. N., et al. 2003, The Astrophysical Journal Supplement Series, 148, 195

Weidenschilling, S. J., & Marzari, F. 1996, Nature, 384, 619

Yee, J. C., Shvartzvald, Y., Gal-Yam, A., et al. 2012, The Astrophysical Journal, 755, 102

Zhu, W., Udalski, A., Calchi Novati, S., et al. 2017, arXiv:1701.05191

List of Publications

1. "OGLE-2015-BLG-1649Lb: A Gas Giant Planet around a Low-mass Dwarf"
   Nagakane, M.; Lee, Chien-Hsiu; Koshimoto, N.; Suzuki, D.; Udalski, A.; Beaulieu, J. P.; Sumi, T.; Bennett, D. P.; Bond, I. A.; Rattenbury, N.; Bachelet, E.; Dominik, M.; Abe, F.; Barry, R. K.; Bhattacharya, A.; Donachie, M.; Fujii, H.; Fukui, A.; Hirao, Y.; Itow, Y.; Kamei, Y.; Kondo, I.; Li, M. C. A.; Matsubara, Y.; Matsuo, T.; Miyazaki, S.; Muraki, Y.; Ranc, C.; Shibai, H.; Suematsu, H.; Sullivan, D. J.; Tristram, P. J.; Yamakawa, T.; Yonehara, A.; MOA Collaboration; Mróz, P.; Poleski, R.; Skowron, J.; Szymański, M. K.; Soszyński, I.; Pietrukowicz, P.; Kozłowski, S.; Ulaczyk, K.; The OGLE Collaboration; Bramich, D. M.; Cassan, A.; Figuera Jaimes, R.; Horne, K.; Hundertmark, M.; Mao, S.; Menzies, J.; Schmidt, R.; Snodgrass, C.; Steele, I. A.; Street, R.; Tsapras, Y.; Wambsganss, J.; The RoboNet Collaboration; Jørgensen, U. G.; Bozza, V.; Longã, P.; Peixinho, N.; Skottfelt, J.; Southworth, J.; Andersen, M. I.; Burgdorf, M. J.; D'Ago, G.; Evans, D. F.; Hinse, T. C.; Korhonen, H.; Rabus, M.; Rahvar, S.; The MiNDSTEp Collaboration
   The Astronomical Journal, Volume 158, Issue 5, article id. 212, 9 pp. (2019).

2. "MOA-2012-BLG-505Lb: A Super-Earth-mass Planet That Probably Resides in the Galactic Bulge"
   Nagakane, M.; Sumi, T.; Koshimoto, N.; Bennett, D. P.; Bond, I. A.; Rattenbury, N.; Suzuki, D.; Abe, F.; Asakura, Y.; Barry, R.; Bhattacharya, A.; Donachie, M.; Fukui, A.; Hirao, Y.; Itow, Y.; Li, M. C. A.; Ling, C. H.; Masuda, K.; Matsubara, Y.; Matsuo, T.; Muraki, Y.; Ohnishi, K.; Ranc, C.; Saito, To.; Sharan, A.; Shibai, H.; Sullivan, D. J.; Tristram, P. J.; Yamada, T.; Yonehara, A.; MOA Collaboration
   The Astronomical Journal, Volume 154, Issue 1, article id. 35, 8 pp. (2017).

List of Presentations

1. “MOA-2015-BLG-404 : 低質量星周りの巨大ガス惑星”
   永金昌幸, MOA コラボレーション
   P301a 日本天文学会 2018 年春季年会, 千葉大学, 2018 年 3 月

2. “低質量 M 型矮星周りを回るスーパーアース : MOA-2012-BLG-505Lb”
   永金昌幸, MOA コラボレーション
   P217a 日本天文学会 2016 年春季年会, 首都大学東京, 2016 年 3 月